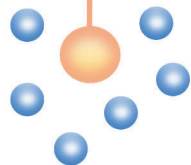


**Weihua Zhang**

# **Multifaceted Applications of Nanocellulose-based Materials for Water Remediation**



**Pollutant**





# Weihua Zhang

Born in 1992, Heze, Shandong, P.R. China

## Previous studies and degrees

B.Sc. Materials Science and Engineering, 2010  
Yantai University, Yantai, Shandong, China

M.Sc. Physical Chemistry of Materials, 2014  
Ocean University of China, Qingdao, Shandong, China

Ph.D. studies at the Laboratory of Natural Materials Technology from October of 2017  
Åbo Akademi University, Turku/Åbo, Finland

# **Multifaceted applications of nanocellulose-based materials for water remediation**

**Weihua Zhang**



Laboratory of Natural Materials Technology, Åbo  
Akademi University, Henrikinkatu 2, Turku FI-20500,  
Finland, 2022

**Supervisors:**

Professor Chunlin Xu  
Laboratory of Natural Materials Technology  
Johan Gadolin Process Chemistry Centre  
Åbo Akademi University  
Åbo, Finland

Professor Stefan Willför  
Laboratory of Natural Materials Technology  
Johan Gadolin Process Chemistry Centre  
Åbo Akademi University  
Åbo, Finland

**Reviewers:**

Professor Henrikki Liimatainen  
Faculty of Technology  
Fibre and Particle Engineering  
University of Oulu  
Oulu, Finland

Associate professor Tiina Nypelö  
Faculty of Chemistry and Chemical Engineering  
All Wood Composite Platform  
Wallenberg Wood Science Center ([wwsc.se](http://wwsc.se))  
Chalmers University of Technology  
Gothenburg, Sweden

**Opponent:**

Professor Henrikki Liimatainen  
Faculty of Technology  
Fibre and Particle Engineering  
University of Oulu  
Oulu, Finland

ISBN 978-952-12-4216-8 (printed)  
ISBN 978-952-12-4217-5 (digital)  
Painosalama Oy — Turku, Finland 2022

*Stay Hungry*

*Stay Foolish*

*To my families*

# Contents

Perface.....	i
List of publications .....	i
Contribution of the author.....	i
Supporting publications, proceedings, and presentations .....	ii
Abstract .....	iii
Keywords .....	iv
Svensk sammanfattning .....	v
Nyckelord.....	vi
List of abbreviations .....	vii
1. Introduction.....	1
1.1 Wastewater treatment.....	1
1.1.1 Heavy metal ions in wastewater .....	1
1.1.2 Organic dyes in wastewater .....	1
1.1.3 Oil-contaminating wastewater .....	2
1.2 Methods for wastewater treatment.....	2
1.3 Aerogel.....	3
1.4 Nanocellulose.....	4
1.4.1 Cellulose .....	4
1.4.2 Nanocellulose.....	5
1.4.3 Preparation of nanocellulose.....	7
1.4.4 Nanocellulose aerogel.....	11
1.4.5 Nanocellulose aerogel for removal of heavy metals from wastewater .....	12
1.4.6 Nanocellulose aerogel for organic dye treatment .....	13
1.4.7 Nanocellulose aerogels for oily wastewater treatment .....	13
2. Hypothesis and objectives of the work .....	15
3. Materials and methods .....	16
3.1 Materials .....	16
3.2 Preparation methods.....	16
3.2.1 Preparation of TEMPO-oxidized CNFs (Paper I, II) .....	16

3.2.2 Preparation of AO-CNFs (Paper III).....	16
3.2.3 Preparation of AO-CNF membrane (Paper III) .....	16
3.2.4 Preparation of CNF/PEI/Ag NPs aerogel (Paper I) .....	17
3.2.5 Preparation of CNF/PEI/ECH aerogel (Paper II).....	17
3.2.6 Preparation of AO-wood aerogel (Paper IV) .....	17
3.3 Characterization methods.....	17
3.3.1 Carbohydrate analysis (Paper IV) .....	17
3.3.2 Spectrometry and microscopy.....	17
3.3.3 Elemental analysis (Paper II, III & IV).....	18
3.3.4 Brunauer-Emmett-Teller (BET) (Paper I, II & IV).....	18
3.3.5 X-ray diffraction (XRD) (Paper III & IV) .....	18
3.3.6 Thermal properties (Paper I).....	18
3.3.7 Zeta-potential (Paper III) .....	19
3.3.8 Mechanical properties .....	19
3.3.9 Catalytic reduction performance (Paper I).....	19
3.3.10 Dye adsorption measurements .....	19
3.3.11 Uranium removal performance measurements .....	20
4. Results and discussion .....	22
4.1 Overview of the thesis work .....	22
4.2 CNF/PEI/Ag NPs aerogels for continuous catalytic discoloration towards organic dyes (Paper I) .....	22
4.2.1 Preparation of CNF/PEI/Ag NPs composite aerogel .....	23
4.2.2 Mechanical stability and shape-recovery in water .....	25
4.2.3 Catalytic discoloration of CNF/PEI/Ag NPs for MB and CR .....	26
4.3 Dual cross-linked CNF/PEI composites for selectively removing anionic dye (Paper II) .....	27
4.3.1 Morphology and properties of the CNF/PEI aerogels .....	28
4.3.2 Shape recovery, water stability, and mechanical performance .....	29
4.3.3 Adsorption and filtration performance in batch.....	30
4.3.4 Regeneration and recyclability .....	31
4.3.5 Selective adsorption and separation.....	32

4.4 Preparation of AO-CNF membrane for uranium adsorption (Paper III) .....	32
4.4.1 Synthesis of AO-CNF .....	33
4.4.2 Adsorption of uranium ions .....	34
4.4.3 Adsorption mechanism .....	36
4.4.4 Filtration performance of the AO-CNF membrane .....	37
4.5 Amidoximated wood aerogel for uranium recovery (Paper IV) .....	38
4.5.1 Preparation of amidoximated wood aerogel .....	38
4.5.2 Properties of the AO-wood aerogel .....	40
4.5.3 Adsorption performance of the AO-wood aerogels for uranium extraction.....	41
4.5.4 Regeneration and reusability.....	44
5. Conclusions and future perspectives.....	47
5.1 Highlights of the thesis .....	47
5.2 Future perspectives .....	47
6. Acknowledgments.....	49
7. References.....	51

## Perface

### List of publications

- I **Weihua Zhang**, Xiaoju Wang, Yongchao Zhang, Basvan Bochove, Ermei Mäkilä, Jukka Seppälä, Wenyang Xu, Stefan Willför, Chunlin Xu, Robust shape-retaining nanocellulose-based aerogels decorated with silver nanoparticles for fast continuous catalytic discoloration of organic dyes. *Separation and Purification Technology* 2020, 242, 116523.
- II **Weihua Zhang**, Luyao Wang, Ermei Mäkilä, Stefan Willför, Chunlin Xu, Ultralight and porous cellulose nanofibers/polyethyleneimine composite aerogels with exceptional performance for selective anionic dye adsorption. *Industrial Crops and Products*, 2022, 177, 114513.
- III **Weihua Zhang**, Xiao Han, Jun You, Xiaofang Zhang, Danfeng Pei, Stefan Willför, Mingjie Li, Chunlin Xu and Chaoxu Li, Rapid and manual-shaking exfoliation of amidoximated cellulose nanofibrils for large-capacity filtration capture of uranium. *Journal of Materials Chemistry A*, 2022, 10, 7920.
- IV **Weihua Zhang**, Chunlin Xu, Xiao Han, Lifen Long, Xinpeng Che, Stefan Willför, Mingjie Li, and Chaoxu Li, Top-Down Approach Making Nanofibril-filled Wood Aerogels for Enhanced Aquatic Uranium Extraction. *Manuscript*.

This work was carried out at the Laboratory of Natural Materials Technology during the years of 2017-2022 under the supervision of Professor Chunlin Xu and Professor Stefan Willför at Åbo Akademi University. Part of the work was carried out at Group of Biomimetic Smart Materials, Qingdao Institute of Bioenergy and Bioprocess Technology, Chinese Academy of Sciences & Shandong Energy Institute, China.

### Contribution of the author

The main author was responsible for planning, experimental work, and writing the articles of **I**, **II**, **III**, and **IV**.

## Supporting publications, proceedings, and presentations

1. Yongchao Zhang, Shuzhen Ni, Xiaoju Wang, **Weihua Zhang**, Lucas Lagerquist, Menghua Qin, Stefan Willför, Chunlin Xu. Ultrafast adsorption of heavy metal ions onto functionalized lignin-based hybrid magnetic nanoparticles. *Chemical Engineering Journal*, 2019, 372, 82-91.
2. **Weihua Zhang**, Xiaoju Wang, Chunlin Xu, Stefan Willför. Robust shape memory nanocellulose based aerogels decorated with silver nanoparticles for dye discoloration. 2019 International Conference on Nanotechnology for Renewable Materials. Chiba, Japan, 3-7 June 2019. (Oral Presentation by Weihua Zhang)
3. Anna Sundberg, Anders Strand, **Weihua Zhang**, Tiffany Abitbol. Preparation and characterization of high-yield cellulose nanocrystals (CNCs) from softwood kraft pulp, International Symposium on Wood, Fiber and Pulp Chemistry - ISWFPC20, September 9-11, 2019, Tokyo, Japan.

## Abstract

During the last decades, water pollution has become a severe environmental and health crisis in many countries due to rapid industrialization and urbanization, attracting increasing attention worldwide. As one of the most common sources of natural polymers, wood-derived materials have caused much attention in water treatment for attributes such as renewability, abundance, non-toxicity, environmentally friendly, and accessibility for derivatization. Therefore, this thesis aimed to develop functional wood-derived materials for wastewater treatment, which is of great significance for both the environment and future biorefinery concepts.

In this thesis, 2,2,6,6-tetramethylpiperidine 1-oxyl (TEMPO) - oxidized cellulose nanofibers (CNFs) were prepared. Then the CNFs were used to fabricate composite aerogel by combining with poly(ethylene imine) (PEI) and silver nanoparticles (Ag NPs). The obtained aerogel with a microporous structure presented excellent catalytic discoloration properties towards organic dyes. Notably, the catalytic activity was very stable, and the discoloration efficiency remained over 98% after 10 times cycles, and the water transportation could reach  $5 \times 10^4 \text{ L m}^{-2} \text{ h}^{-1}$ . In addition, the composites also exhibited rapid water-activated shape memory, and the structure kept its integrity over an extended period of time.

Then the TEMPO-CNFs were also used to prepare porous and ultralight aerogel with PEI via physical and chemical cross-linking with epichlorohydrin (ECH). The results revealed that the dual cross-linked composite aerogel exhibited superior water resistance in different water environments, fast water-activated shape memory, and rapid water transportation. Most impressively, the CNF/PEI aerogel with a weight ratio at 1:2 showed excellent performance for removing methyl orange (MO) in batch ( $1226 \text{ mg g}^{-1}$ , pH 6). Moreover, the aerogel presented outstanding selective separation performance.

Furthermore, we firstly produced a novel type of nanocellulose through exfoliation of amidoximated cellulose nanofibers (AO-CNF) from commercial softwood pulp. Both morphology and the abundant active adsorption sites endow excellent performance for extracting uranium ions. The obtained AO-CNF exhibited excellent uranium uptake in batch ( $1327 \text{ mg g}^{-1}$ ) at pH 8. Moreover, AO-CNF can also be used to construct nanofibrous membranes via vacuum filtration. In the case of a  $2.5 \text{ }\mu\text{m}$  thick membrane it could afford an ultra-high flux of  $\sim 48 \text{ L m}^{-2} \text{ h}^{-1}$  with high treatment efficiency (99.9%).

Lastly, natural wood was directly used to fabricate highly mesoporous wood aerogels through cyanoethylation and amidoximation. The obtained amidoximated wood (AO-wood) exhibited excellent mechanical performance and high surface area. The adsorption capacity towards uranium was high over a wide pH value, and the highest uptake ability was as high as  $1375 \text{ mg g}^{-1}$ .

More importantly, the AO-wood's unique structure can make it a filter to remove uranium ions efficiently by filtration.

Therefore, the studied wood-derived functional materials exhibit great potential for wastewater treatment.

## **Keywords**

nanocellulose, wood, discoloration, organic dyes, adsorption, uranium extraction, aerogel, membrane, filtration, wastewater treatment, amidoximation

## Svensk sammanfattning

Under de senaste decennierna har vattenföroreningar blivit en allvarlig miljö- och hälsokris i många länder på grund av snabb industrialisering och urbanisering, vilket har väckt ökad uppmärksamhet över hela världen. Som en av de vanligaste källorna till naturliga polymerer har trähärledda material fått ökad uppmärksamhet vid vattenbehandling för egenskaper som förnyelsebarhet, överflöd, icke-toxicitet, miljövänlighet och tillgänglighet för derivatisering. Därför strävade avhandlingen till att utveckla funktionella trähärledda material för avloppsvattenrening, vilket är av stor betydelse för både miljön och framtida bioraffinaderikoncept.

I denna avhandling har 2,2,6,6-tetrametylpiperidin 1-oxyl (TEMPO) -oxiderade cellulosanofibrer (CNF) framställts. Sedan användes CNF för att tillverka komposit aerogel genom att kombinera med poly(etylenimin) (PEI) och silver nanopartiklar (Ag NPs). Den erhållna aerogelen med mikroporös struktur uppvisade utmärkta katalytiska missfärgningsegenskaper mot organiska färgämnen. Noterbart var att den katalytisk aktiviteten var mycket stabil, och missfärgningseffektiviteten förblev över 98% efter 10 cykler, och vattentransporten kunde nå  $5 \times 10^4 \text{ L m}^{-2} \text{ h}^{-1}$ . Dessutom uppvisade kompositerna också ett snabbt vattenaktiverat formminne, och strukturen bevarade sin integritet under en längre period.

Sedan användes TEMPO-CNF också för att tillverka mycket porös och ultralätt aerogel med PEI via fysisk och kemisk korsbindning med epiklorhydrin (ECH). Resultaten visade att den dubbelt korsbundna kompositaerogelen uppvisade överlägsen vattenresistens i olika vattenmiljöer, snabbt vattenaktiverat formminne och snabb vattentransport. Mest imponerande visade CNF/PEI aerogelen med ett viktförhållande på 1:2 utmärkt prestanda för avlägsnande av metylorange (MO) i sats ( $1226 \text{ mg g}^{-1}$ , pH 6). Dessutom uppvisade aerogeln enastående selektiv separationsprestanda.

Dessutom producerade vi först en ny typ av nanocellulosa genom exfoliering av amidoximerade cellulosanofibrer (AO-CNF) från kommersiell barrvedsmassa. Både morfologin och de rikliga aktiva adsorptionsplatserna ger utmärkt prestanda för utvinning av uranjoner. Den erhållna AO-CNF uppvisade utmärkt uranupptag i sats ( $1327 \text{ mg g}^{-1}$ ) vid pH 8. Dessutom kan AO-CNF också användas för att konstruera nanofibrösa membran via vakuumfiltrering. När det gäller ett  $2,5 \mu\text{m}$  tjockt membran klarade det ett ultrahögt flöde på  $\sim 48 \text{ L m}^{-2} \text{ h}^{-1}$  med en avlägsnandeeffektivitet nära 99,9%.

Slutligen användes naturligt trä direkt för att tillverka mycket mesoporösa träaerogeler genom cyanoetylering och amidoximering. Det erhållna amidoximerade träet (AO-trä) uppvisade utmärkt mekanisk prestanda och hög yta. Adsorptionskapaciteten mot uran var hög över ett brett pH-värde och högsta upptagningsförmåga var så hög som  $1375 \text{ mg g}^{-1}$ . Ännu viktigare, AO-träets

unika struktur kan göra det till ett filter för att avlägsna uranjoner effektivt genom filtrering.

Därför har träbaserade funktionella material stor potential inom området avloppsvattenrening.

## **Nyckelord**

nanocellulosa, trä, missfärgning, organiska färgämnen, adsorption, uranextraktion, aerogel, membran, filtrering, avloppsrening, amidoximering

## List of abbreviations

AFM	Atomic force microscopy
AN	Acrylonitrile
Ag NPs	Silver nanoparticles
AN-wood	Cyanoethylated-wood
AO-CNF	Amidoximated cellulose nanofibers
AO-wood	Amidoximated wood
BC	Bacterial cellulose
BET	Brunauer-emmett-teller
CNC	Cellulose nanocrystals
CNFs	Cellulose nanofibers
CR	Congo red
DS	Degree of substitution
ECH	Epichlorohydrin
FTIR	Fourier transform infrared spectroscopy
HPLC	High-performance liquid chromatography
IC	Indigo carmine
MB	Methylene blue
MG	Malachite green
MMB	Methylthymol blue
MO	Methyl orange
MOF/COF	Metal/covalent-organic frameworks
MTMS	Methyltrimethoxysilane
MTPS	3-mercaptopropyl-trimethoxysilane
NREL	National renewable energy laboratory
PAE	Polyamideamine-epichlorohydrin
PEI	Poly(ethylene imine)
RB	Rhodamine B
SEM	Scanning electron microscopy
TEMPO	2,2,6,6-Tetramethylpiperidine 1-oxyl
TEM	Transmission electron microscopy
TMCS	Chlorotrimethylsilane
TG	Thermal gravimetric analyzer
XPS	X-ray photoelectron spectroscopy
XRD	X-ray diffraction

# **1. Introduction**

## **1.1 Wastewater treatment**

Water is an essential natural resource for human beings. Our world currently faces a global water challenge and increasing amount of wastewaters are produced and discharged into the environment owing to the rapid industrialization. The contamination of underground and surface water caused by the discharge of non-compliant wastewater has become a severe environmental problem, which has caused severe problems to water resources, soil, and even air.[1-3] Nowadays, smelting, electronics, mining, medicine, papermaking, printing, and other industries have produced a large amount of wastewater containing organic, oil, inorganic, heavy metals, pathogens, and other pollutants.[4-9] Once these pollutants enter the natural water, and they will cause physical, chemical, and biological changes of the water body and result in the deterioration of water quality. These pollutants would furthermore enter and accumulate in the human body eventually and induce varying degrees of damage to human health.[10-12]

### **1.1.1 Heavy metal ions in wastewater**

Metals with a density of over  $4.5 \text{ g cm}^{-3}$  are usually named heavy metals, including copper (Cu), lead (Pb), gold (Au), cadmium (Cd), mercury (Hg), uranium (U), and nickel (Ni), etc.[13, 14] Heavy metal ions are mainly produced from mining, metallurgy, chemical industry, electronics, leather, paper, and other industries. Once they are discharged into the environment, they can cause serious pollution to water and soil.[14, 15] Among these heavy metals, uranium ions have caused more and more people's attention on account of their potential threats e.g., lethal toxicity and radioactivity. The heavy metal elements have excellent properties of migration, enrichment, and concealment, and they can enter the human body through air, water, or the food chain. Heavy metal ions are very harmful because of their significant biological toxicity, which can cause chronic poisoning. In addition, they have a bad effect on the immune system due to their carcinogenic, teratogenic, and mutagenic effects.[16] Once the heavy metal ions enter the environment, they would experience various physical and chemical processes, such as precipitation-dissolution, redox, coordination, colloid formation, adsorption-desorption, etc. Finally, they would stay in the environment in different forms, causing permanent potential hazards.[17]

### **1.1.2 Organic dyes in wastewater**

Various organic dye-contaminating wastewaters are mainly discharged from printing and dyeing factories that produce and process cotton, hemp, chemical fiber, and silk.[18, 19] In recent years, the printing and dyeing industry has developed rapidly, and the amount of discharged wastewater has been strongly increasing year by year. Most organic dyes have a complex aromatic molecular structure, especially synthetic dyes, and they are difficult to be degraded

naturally in water environment for they have strong stability to heat, light, and oxidants and excellent solubility in water.[20, 21] Once these organic dyes are directly discharged into the environment, they will cause various damages to animals and plants because they will block the penetration of sunlight, reduce the aquatic plants' photosynthetic efficiency, and eventually break the balance of ecosystems.[3, 22, 23] In addition, organic dyes may also accumulate in the animal body, resulting in diverse serious health problems due to their mutagenic or carcinogenic.[23]

### **1.1.3 Oil-contaminating wastewater**

Oily wastewater is also one of the main components of industrial wastewaters. Increased volume of oily wastewater is produced from fats, hydrocarbons and diesel, gasoline, food, beverages, and oil spills.[24, 25] For example, in 2010, more than 210 million gallons of crude oil was disposed into the Gulf of Mexico, which resulted in various problems to the ecological balance.[26] Oily wastewater usually contains toxic chemicals, which have potential harm to human beings not only for their carcinogenic and mutagenic effects but also due to their inhibitory effect on plant growth. If the discharge of oily wastewater is not properly treated, it will form a layer on the water surface to reduce the penetration of sunlight to the water body, thereby destroying the aquatic ecology system. Therefore, the treatment of oily wastewater is crucial for reducing its impact on the environment and humans.

## **1.2 Methods for wastewater treatment**

At present, the main treatment methods for wastewater are biological, chemical oxidation, photocatalytic oxidation, membrane separation, and adsorption.[27-31] Biological methods refer to the use of microbial metabolism to degrade organic matter to achieve the purpose of removing organic pollutants in sewage. Chemical oxidation refers to the use of a strong oxidizing agent to degrade the pollutants in the water. Photocatalytic oxidation refers to the use of ultraviolet and visible light to remove pollutants in water through the oxidation of catalysts. Membrane separation mainly includes microfiltration, ultrafiltration, and reverse osmosis, and purifies wastewater by separating, concentrating, and recycling pollutants in various industrial wastewaters. The adsorption method refers to the use of an adsorption material with certain amount of pores and large specific surface area to remove the contaminants in the wastewater by adsorption. However, the microbial reproduction speed and reaction rate of the biological method is usually slow, and the treated water is difficult to reuse; the chemical oxidation often requires the use of some chemicals, which is prone to secondary pollution; the photocatalytic oxidation is not effective in treating high-concentration printing and dyeing wastewater; the operation and maintenance cost of the membrane separation method is relatively high, and the membrane is susceptible to pollution, resulting in reduced performance and limited flow. The adsorption method has been favored recently because of its

easy operation, high efficiency, cheap, fewer chemical reagents, and environmental friendliness.

The present conventional and advanced approaches for treating the increasing contaminants in water are limited for the lack of adaptive technological tools. The main disadvantages of the technologies for removing pollutants from wastewater are high-energy consumption, fouling of microorganism, and low removal efficiency for new pollutants.[32] Nowadays, these technologies cannot be used widely all over the world, and only some of these technologies were applied in several countries all over the world.[33] In addition, the amount of the contaminants are increasing and new contaminants are emerging in water bodies due to rapid industrialization. Therefore, developing novel materials to treat wastewater is essential.

### 1.3 Aerogel

Since Kistler introduced aerogels to the world in 1931, they have caused increasing interest as immersing materials in wastewater treatment for their porous micro- or nanostructure.[34, 35] Aerogels are regarded as the lightest solid materials (90–99% air), and provide a simple, low-cost, green, and safe technology for water cleaning.[36] They are usually produced from polymer-based gels using different drying methods aiming at light weight and large specific surface area. The main classifications of aerogels are organic, inorganic, and composite aerogels according to the starting materials.[37] The aerogel can be further classified into aerogels, xerogels, and cryogels produced from supercritical drying, ambient pressure-drying, and freeze-drying, respectively. In addition, the polarity and surface functionality can be tuned into hydrophilic, hydrophobic, amphiphilic, oleophilic, or oleophobic through different physical or chemical strategies.[38]

The most common raw materials for preparing organic aerogel are synthetic polymers (melamine-formaldehyde, polyacrylamides, polyacrylates, polyurethanes, polyvinyl alcohol dialdehyde, etc.), and natural polymers (chitosan, starch, cellulose, alginate, gelatin, agar).[39, 40] The common starting materials for preparing inorganic aerogels are transition metal oxides/metals (silica,  $\text{Al}_2\text{O}_3$ ,  $\text{SnO}_2$ , etc.), chalcogenides ( $\text{CdS}$ ,  $\text{CdSe}$ ), and carbon materials (graphene, carbon nanotube, and carbonized polymers).[41–43] Composite aerogels are usually produced by combining organic and inorganic materials, which inherit the advantages of the organic and inorganic aerogels.[44]

Aerogels have been developed widely as a matrix to support various novel materials such as semiconductors, metal-organic frameworks (MOF), oxides, polymers, and metal, ascribed to their porous structure, low density, and large specific surface area.[44, 45] These composite aerogels showed diverse applications in the field of wastewater treatment, such as dye removal, oil/water separation, toxic metal ions removal, organic pollutants degradation, and

photothermal evaporation.[46-50] The main types of aerogels and their applications in wastewater treatment are presented in **Figure 1.1**.

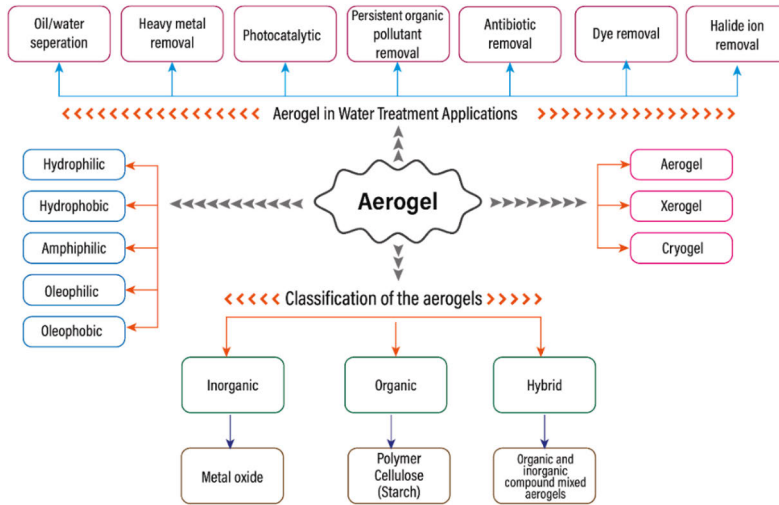


**Figure 1.1.** Classification and applications of aerogels. (Copyright by Elsevier, 2021, [51])

## 1.4 Nanocellulose

### 1.4.1 Cellulose

As a natural polymer compound, cellulose widely exists in plants, bacteria, and algae. Since Anselme Payen firstly discovered and isolated cellulose in 1838, its biosynthetic process, physicochemical properties, and structural characteristics have been widely studied, promoting the development of related disciplines[52, 53]. The molecular formula of cellulose is  $(C_6H_{10}O_5)_n$  ( $n$  is the degree of polymerization). **Figure 1.2** presents that the cellulose molecule is a linear chain of  $\beta$ -(1-4)-linked anhydroglucose (AGU) repeating units from several hundred to ten thousand.[54] The cellulose molecule chains contain numerous hydroxyl groups on the glucopyranose ring, and these active hydroxyl groups are easy to form intramolecular and intermolecular hydrogen bond connections (**Figure 1.2**). The stable network structure formed through these inter-/intra hydrogen bonds between cellulose molecule chains can enhance the rigidity of the cellulose molecular chain and contribute to form a dense crystalline region. In addition to the crystalline region, some cellulose molecular chains are arranged loosely and irregularly, and their tendency is roughly parallel to the cellulose axis to form the amorphous region (**Figure 1.2**).[55, 56]

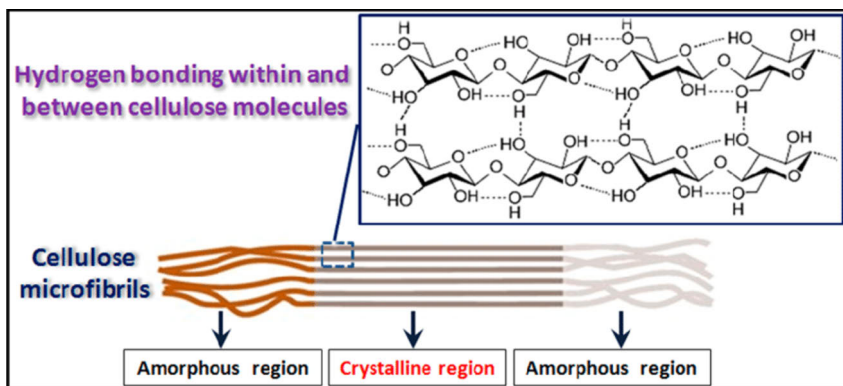


**Figure 1.2.** Schematic representation of interaction between cellulose molecular chains, and the amorphous region and crystalline region of cellulose microfibrils. (Copyright by Neralla, S. (Ed.), 2012,[57])

## 1.4.2 Nanocellulose

Nanocellulose, a kind of nanostructured cellulose material extracted from natural biomass, has been studied widely for its excellent mechanical performance, biodegradability, large specific surface area, and high reactivity.[58] Because of these unique properties, nanocellulose has demonstrated significant current and potential future applications in food[59], medical[60], water treatment[61], clothing[60], papermaking[62], electronics[63], etc. Therefore, nanocellulose has become a research hotspot in recent years. Based on the difference in size, morphology, and preparation method, nanocellulose is usually classified into the following three main types: cellulose nanocrystals (CNC), cellulose nanofibers (CNF), and bacterial cellulose (BC) (Figure 1.3 and Table 1.1).[64]

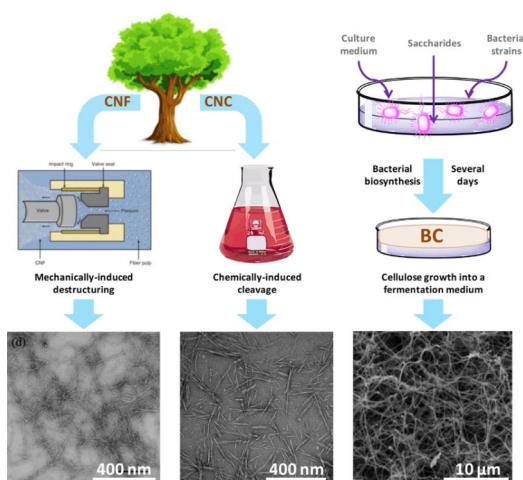


**Figure 1.3.** Scheme showing commonly followed routes to nanocellulose fabrication. (Copyright by Elsevier, 2020,[65])

CNC is mainly derived from natural plant fibers such as wood, bamboo, and crop stalks, and is usually produced by strong acid hydrolysis. CNC has rod-like or spherical morphology (diameter: 5~70 nm, length: 100~250 nm), and high modulus and crystallinity[66]. CNF is usually prepared by mechanical methods or in combination with chemical methods from natural plant fibers such as wood, sugar beet, flax, etc., with irregular entanglement of fibrils (diameter: 5~70 nm, length: several micrometers) and a relatively low crystallinity[67]. BC is usually synthesized by a specific bacterium (e.g., *Gluconacetabacter xylinus*). The bacterial cell synthesizes the glucose chain, which is then squeezed from the pores of the cell membrane. Several glucose chains further form microfibrils, which are intertwined to form a three-dimensional nanostructured network of cellulose fibers.[68]

**Table 1.1.** *The classifications, sources, and properties of nanocellulose. (Copyright by John Wiley and Sons, 2011,[64])*

Type of nano-cellulose	Selected references and synonyms	Typical sources	Formation and average size
CNF	Microfibrillated cellulose, cellulose nanofibrils and microfibrils, nanofibrillated cellulose	wood, sugar beet, potato tuber, hemp, flax	Delamination of wood pulp by mechanical pressure before and /or after chemical or enzymatic treatment diameter:5–60nm length: several micrometers
CNC	Cellulose nanocrystals, crystallites, whiskers, rodlike cellulose microcrystals	Wood, cotton, hemp, flax, wheat, straw, mulberry bark, ramie, Avicel, tunicin, cellulose from algae and bacteria	Strong acid hydrolysis of cellulose from many sources  Diameter:5–70nm Length:100–250nm (from plant celluloses); 100nm to several micrometers (from celluloses of tunicates, algae, bacteria)
BC	Bacterial cellulose, microbial cellulose, biocellulose	Low-molecular-weight sugars and alcohols	Bacterial synthesis  Diameter: 20-100nm;different types of nanofiber network

### 1.4.3 Preparation of nanocellulose

Because of the existence of Van der Waals forces and hydrogen bonds between cellulose molecule chains, extracting nano-sized and high-quality nanocellulose from natural cellulose still needs to be broken through in the biorefinery field. To this day, various approaches were developed for nanocellulose preparation, including mechanical disintegration (homogenization, grinding, refining, extrusion, blending, ultrasonication, cryocrushing, steam explosion, ball milling, and aqueous counter collision), biological and chemical pretreatments (enzymatic hydrolysis, TEMPO oxidation,  $\text{NaIO}_4/\text{NaClO}_2$  oxidation, sulfonation, carboxymethylation, quaternization), and microbial synthesis.[67] At present, the common methods for preparing nanocellulose are inorganic acid hydrolysis, TEMPO/ $\text{NaClO}/\text{NaBr}$  oxidation, high-pressure homogenization, mechanical grinding, and microbial synthesis.[67-69]

#### 1.4.3.1 Mineral acid hydrolysis

In the 1840s, Nickerson and Habrle prepared CNC colloidal suspension through hydrochloric acid and sulfuric acid hydrolysis.[70] A few years later, Ranby et al. prepared CNC with sulfuric acid.[71] Until now, sulfuric acid hydrolysis is still the main method to produce CNC. Sulfuric acid hydrolysis of cellulose is mainly to break the cellulose glycosidic bond, combine the sulfonic acid group with the free hydroxyl group on cellulose molecules' chain, increase the solution's negative electricity, and reduce the degree of polymerization of cellulose macromolecules (**Figure 1.4**). The CNC obtained from this method usually has low thermal stability and good dispersion. The highest yield of CNC could be obtained at the controlled conditions (acid concentration from 63 to 64 wt%, temperature from 45 to 60 °C, and reaction time from 30 to 120 min.[72, 73]). When the acid concentration is over 64 wt%, partial degradation of crystalline regions will occur.[73] As a result, the diameter size of the produced CNC is 2.3–60 nm, the length is 100~500 nm, with high crystallinity.[74, 75] Moreover, the CNC can also be produced through hydrochloric acid hydrolysis, which has poor dispersion in water and is easy to agglomerate into flocs.[76] Mixed acids, such as HCl,  $\text{HNO}_3$ , and  $\text{H}_3\text{PO}_4$ , can also be used to produce CNC.[75] Cheng et al. presented a one-step hydrolysis procedure to prepare CNC with the mixture of HCl and  $\text{HNO}_3$  with a volume ratio at 7:3 under 110 °C with a reaction time of 180 min. In this method, the primary hydroxyl group of cellulose was replaced with carboxyl groups, and the CNC can be obtained within a short time, high-yield, and dispersion stability.[77] The main influencing factors for the inorganic acid hydrolysis process are raw material, classification, concentration, hydrolysis temperature, reaction time, acid/pulp ratio and so on.

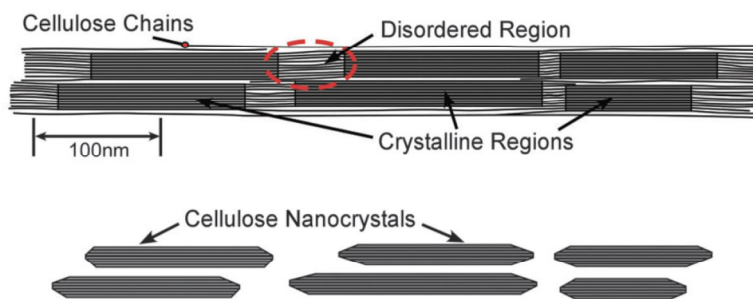


**Figure 1.4.** Schematic representation of the process for the preparation via acid hydrolysis. (Copyright by Progress in Chemistry, 2021[78])

### 1.4.3.2 TEMPO/NaClO/NaBr oxidation

Since 1993, Davis and Flitsch reported that the primary -OH group on the cellulose chain can be selectively oxidized into -COOH by TEMPO radicals. Since then this method has been studied widely to produce CNFs.[79] Saito et al. prepared CNFs with the carboxyl content reach to  $1.52 \text{ mmol g}^{-1}$  by using this method. In brief, different types of never-dried cellulose pulp were oxidized under ambient conditions for a few hours. After washing, they were disintegrated into individual nanofibrils by blending and the diameter size was in the range of 3–5 nm.[80] The mechanism of TEMPO/NaClO/NaBr oxidation to prepare CNFs is to selectively oxidize the hydroxyl group on C6 into aldehydes and then oxidize into carboxylic groups by the  $\text{NO}^+$ , produced in situ in the process of the reaction between TEMPO radical and the oxidants (**Figure 1.5**).[81] However, in the alkaline solution, the aldehyde group left over from the chemical reaction will reduce the dispersion of cellulose, decrease its dispersion stability, and change the color at high temperatures.[82, 83] To develop energy-efficient ways for producing CNFs, TEMPO and its derivatives have been developed and lots of works were carried out, particularly in the group of Prof. Akira Isogai.[81]

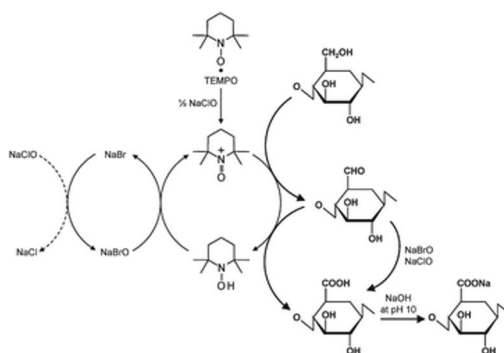


**Figure 1.5.** Schematic representation of the process for the C6 primary hydroxyls of cellulose to C6 carboxylate groups during TEMPO/NaBr/NaClO oxidation in water at pH 10–11. (Copyright by Royal Society of Chemistry, 2011[81])

### 1.4.3.3 High-pressure homogenization

Homogenizers and microfluidizers are the two main types of high-pressure homogenization equipment and are used widely in the field of food, cosmetics, pharmacy, and biotechnology. In 1983, Herrick first produced CNFs by passing the 2 wt.% wood pulp suspension through a Manton-Gaulin homogenizer.[84] Based on this work, more and more researchers have tried to optimize and improve the high-pressure homogenization approach for nanocellulose production. The working principle of the high-pressure homogenization is that the cellulose pulp suspension passes through the tiny gap between the homogenizing valve and the impact ring (**Figure 1.6**). When the pulp fibers pass through the homogeneous chamber, they can be fibrillated due to the huge shear and impact forces. This process can be repeated as many as dozens of times to ensure cellulose fibrillation. In addition, a microfluidizer (Microfluidics Inc., USA) was also shown by Zimmermann to prepare CNFs as an alternative to homogenizer (**Figure 1.6**).[85] In brief, sulphite pulp suspensions were stirred for 8 h under 24,000 rpm and then passed through an M-100Y microfluidizer processor under 1000 bar for 60 min. Consequently, cellulose nanofibrils with a diameter from 20 to 100 nm and a length with several tens of micrometers were produced. For a long-time, high-energy consumption (70 MW h/t) and the blocking of the system are the two main barriers to the commercial success of homogenization. To avoid these problems, the cellulose pulp can be pretreated first (e.g., enzymatic or oxidation), which can decrease the high energy consumption dramatically to 2 MW h/t and reduce the risk of blocking.[86]

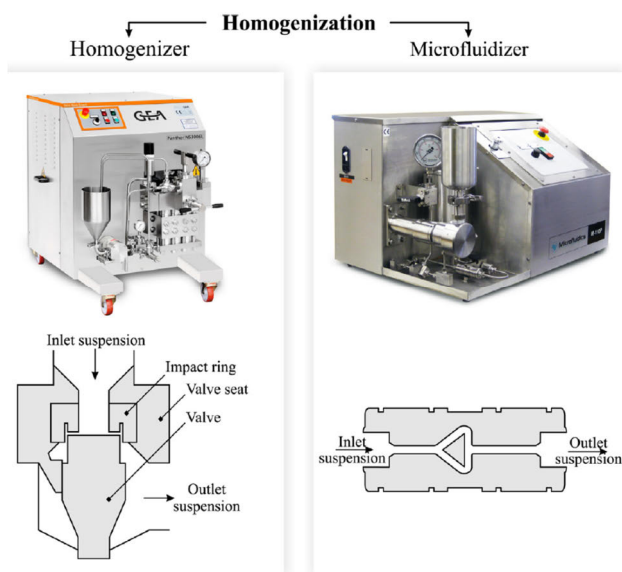


**Figure 1.6.** Mechanical processes for CNF production. (Copyright by Elsevier, 2016[67])

#### 1.4.3.4 Microbial synthesis

BC is a kind of nanocellulose that is entangled with microfibrils produced by bacterial metabolism (**Figure 1.7**).[87] BC produced from bacteria was firstly reported by Brown in 1886. Since then, more and more works found that cellulose was synthesized from diverse bacteria, including gram-negative bacteria species (*Acetobacter azotobacter*, *rhizobium*) and gram-positive bacterial species (*Sarcina ventriculi*).[88, 89] Although plant-based cellulose and BC are all produced from nature, there are still significant differences between them, like purity, macromolecular properties, and characteristics. Generally, BC exhibits relatively high crystalline, excellent mechanical strength, high water uptake capacity, high specific surface area and aspect ratio compared with that of plant-based cellulose, as is shown in **Table 1.2**. [68]

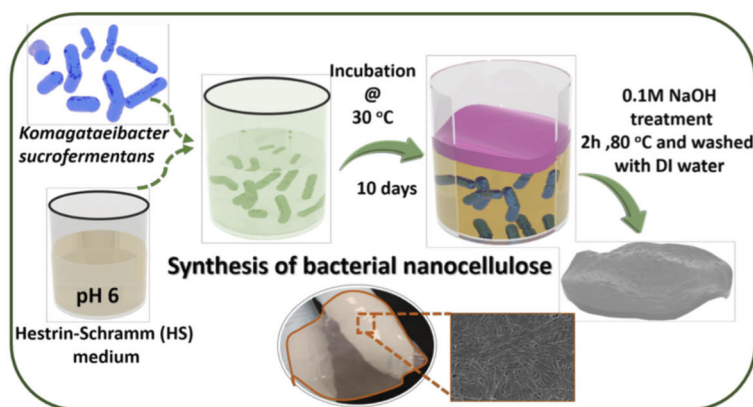


**Figure 1.7.** Bacterial nano-cellulose production from *K. sucrofermentans*. (Copyright by Springer, 2020[90])

**Table 1.2** The difference of the physical properties for bacterial and plant-based cellulose. (Copyright by Elsevier, 2019[68])

Properties	BC	PC
Tensile strength (MPa)	20-300	24-200
Young's modulus (MPa)	Sheet: 20,000 Single fibre: 130,000	2.5-0.170
Water holding capacity (%)	> 95	25-35
Size of fibers (nm)	20-100	Micrometer scale
Crystallinity (%)	74-96	40-85
Relative hydrophilicity (%)	40-50	20-30
Purity (%)	> 99	< 80
Degree of polymerization	14000-16000	300-10000
Porosity (%)	> 85	< 75
Total surface area (m <sup>2</sup> /g)	> 150	< 10

#### 1.4.4 Nanocellulose aerogel

As an emerging material, nanocellulose aerogels have all the characteristics of traditional aerogels (large specific surface areas and high porosity) (**Figure 1.8**). Besides, nanocellulose aerogel also exhibits extremely low density and better ductility compared with traditional organic or polymer aerogels. Therefore, nanocellulose aerogel has been developed and applied widely in various fields. Various cellulose sources and preparation processes may give nanocellulose aerogel materials with completely different properties. “Top-Down” and “Bottom-Up” approaches are the two main ways to fabricate nanocellulose aerogel. Generally, solvent-regenerated nanocellulose aerogel and cellulose nanofibril aerogel are the common “top-down” types of nanocellulose aerogels. Regenerated nanocellulose aerogel is usually prepared by freeze-drying or supercritical carbon dioxide drying, which can prevent the pore structure collapse during the drying process. Therefore, the prepared aerogel usually presents high specific surface area and porosity. However, the solvent of regenerated cellulose is relatively expensive and toxic, and its ability to disperse cellulose polymers is also limited. In comparison, natural cellulose nanofibers can be well dispersed in the water phase, and the aerogel is obtained by freeze-drying or supercritical carbon dioxide drying, and the samples possess the advantages of being environmentally friendly and easily available. However, “bottom up” approach is time and energy consuming, because the nanocellulose is extracted from various sources and undergo treatments by reconstructing of the building blocks to form aerogels. In recent years, “top-down” approach as an alternative approach for preparing nanocellulose aerogel have been studied widely, which can take advantage of the intrinsic porous structure of natural wood without the reconstructing process. Therefore, natural wood with anisotropic and highly elongated cells has been utilized widely as starting material to prepare nanocellulose aerogels. Delignification (e.g., partial dissolution with  $\text{Na}_2\text{SO}_3$ ,  $\text{H}_2\text{O}_2$  or  $\text{NaClO}$ ) [91, 92] and further treatment (e.g., TEMPO-mediated oxidation) [93, 94] can expose more cellulose nanofibrils from the cell walls (i.e., matrix of hemicellulose and lignin), and thereby increase the specific surface area and porosity of the wood-based nanocellulose aerogels. Furthermore, nanocellulose aerogel is easy to undergo a variety of chemical surface modifications to achieve various functions due to the abundant hydroxyl groups on its surface.

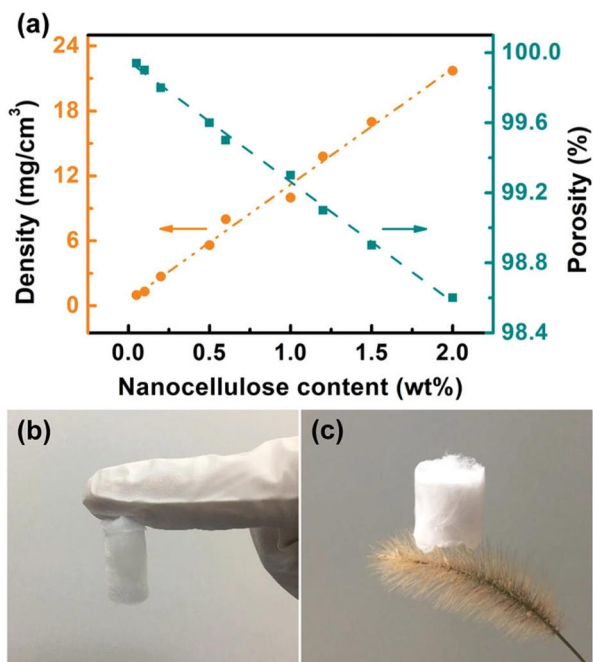


**Figure 1.8.** (a) The relationship of density and porosity VS nanocellulose content of the aerogel. Images showed the ultralight CNF aerogel with contents of 0.05 wt% (b) and 0.5 wt% (c). (Copyright by John Wiley and Sons, 2021[95])

#### 1.4.5 Nanocellulose aerogel for removal of heavy metals from wastewater

Nanocellulose aerogels have attracted increasing interest for capturing various heavy metal ions from wastewater. However, nanocellulose aerogel usually shows limited performance for treating heavy metals because of the surface groups and weak wet stability in working conditions. To improve the performance of the nanocellulose aerogels, nanocellulose was usually combined with other polymers such as chitosan,[96] alginate,[97] PEI,[98] PVA,[99] etc., as well as with various nanoparticles  $\text{Fe}_3\text{O}_4$ , [100] GO,[101] MOF,[102] hydroxyapatite,[103] etc. Li et al. fabricated CNF/PEI composite aerogel through electrostatic combination, which showed excellent water stability and water-activated shape recovery. The maximum adsorption capacity towards  $\text{Cu}^{2+}$  and  $\text{Pb}^{2+}$  was  $175.44 \text{ mg g}^{-1}$  and  $357.44 \text{ mg g}^{-1}$ , respectively.[104] Geng et al. reported a thiol-functionalized nanocellulose aerogel obtained by freeze-drying of a CNF suspension mixed with hydrolyzed 3-mercaptopropyl-trimethoxysilane (MPTS) sols. The obtained samples could remove 92%  $\text{Hg}^{2+}$  ions within the  $\text{Hg}^{2+}$  concentrations from 0.01 to  $85 \text{ mg L}^{-1}$ , and the maximal adsorption capacity reached  $718.5 \text{ mg g}^{-1}$ . [105] Nanocellulose composite aerogel was also obtained by combining with ferromagnetic oxide nanoparticles, which showed excellent treatment efficiency for chromium ions.[106] The resulting composite aerogel presented excellent saturation magnetization of  $53.69 \text{ emu g}^{-1}$ , which is beneficial to recover the aerogel effectively and easily with magnetic.

#### 1.4.6 Nanocellulose aerogel for organic dye treatment

More and more researchers reported nanocellulose-based aerogels for treatment of organic dye-contaminating water through adsorption, filtration, catalytic reduction, and degradation.[95, 107-110] Among the above technologies, adsorption was regarded as one of the most effective approaches due to its high efficiency, low cost, and easy operation. Therefore, various nanocellulose based aerogels were produced by combining with other polymers (chitosan, alginate, and PEI)[111-113] and nanoparticles (noble metal, GO, and MOF) for the dye-containing wastewater.[107, 114] Zhu et al. prepared shapeable fibrous aerogels of CNF/MOF composite aerogel with in situ growing MOF crystals on the CNF template. The obtained aerogel exhibited excellent mechanical flexibility, prevented the aggregation possibilities of MOF crystals, and achieved higher adsorption capacity and rapid adsorption kinetics towards different organic dyes compared to conventional MOF powders.[107] Gu et al. fabricated highly porous CNF/Pd NPs aerogels, which showed excellent catalytic discoloration of dyes solutions in batch and dynamic flow process with a high discoloration efficiency (91–99%).[115] Ma et al. prepared g-C<sub>3</sub>N<sub>4</sub>@nanocellulose composite aerogel for photocatalytic degradation of dyes by using a facile chemical cross-linking method. The composite aerogel exhibited excellent photocatalytic efficiency (99.0%) towards MO with high recyclability and structural stability.[110]

#### 1.4.7 Nanocellulose aerogels for oily wastewater treatment

As known, nanocellulose exhibits excellent underwater hydrophilic and oleophobic performance because of the abundant hydroxyl groups on its surface. Therefore, nanocellulose can be applied for fabricating aerogel filters to separate oil-water mixtures or emulsions. He et al. prepared a hydrophilic CNF aerogel filter by crosslinking with Polyamideamine-epichlorohydrin (PAE). The separation efficiency of the aerogel filter for the oil-water mixture reached nearly 100% even after 10 repeated tests, and the separation efficiency for emulsion reached 98.6%. In addition, nanocellulose aerogel can also be used as adsorbent materials for removing oil from wastewater. At present, the main strategy is the hydrophobic treatment of the nanocellulose aerogel using silane coupling agents such as chlorotrimethylsilane (TMCS) and methyltrimethoxysilane (MTMS).[47, 116, 117] [118] Zhang et al. prepared hierarchical porous BC aerogel by an interfacial engineering strategy to obtain mineral-coated nanocellulose superhydrophobic composite aerogels by mixing nanocellulose and MTMS followed by freeze-drying. The aerogel presented excellent mechanical compressibility in a wide range of temperatures, superhydrophobicity performance ( $\approx 168^\circ$ ), and effective oil/water separation. Sai et al. reported superhydrophobic nanocellulose aerogel modified with TMACS, which showed low density ( $\leq 6.77 \text{ mg cm}^{-3}$ ), large specific surface area ( $\geq 169.1 \text{ m}^2 \text{ g}^{-1}$ ), and high porosity ( $\approx 99.6\%$ ). Moreover, the contact angle reached  $146.5^\circ$  and the oil uptake capacity was up to  $185 \text{ g g}^{-1}$ . Korhonen et al. fabricated hydrophobic nanocellulose composite aerogel by depositing TiO<sub>2</sub> hydrophobic

layer on the nanocellulose aerogel surface by vacuum freeze-drying. The materials showed rapid adsorption performance and excellent reusability after continuous oil adsorption tests.

## 2. Hypothesis and objectives of the work

The main hypothesis of this thesis was that wood, especially cellulose, could be used as the starting material to develop wood-derived functional materials for wastewater treatment applications ascribed to their properties such as abundance in nature, renewability, degradability, and derivatization. Therefore, this work was planned to fabricate different wood-based composite materials for wastewater treatment, which may have great significance for both the environment and future biorefinery concepts.

The first objective was to fabricate CNF/PEI/Ag NPs aerogel for continuous catalytic discoloration of organic dyes by filtration. Then the CNF/PEI aerogels were cross-linked with ECH and used for selective adsorption, filtration, and separation of organic dyes. **(Paper I & II)**

The second objective was to prepare novel CNF adsorbents from different biomass resources through covalent modification and hydrolysis in the forms of suspension or aerogel. The degree of substitution (DS) and hydrolysis time was assumed to be controlled during preparation. The adsorption performance of these CNF adsorbents towards uranium ions was studied. **(Paper III & IV)**

### 3. Materials and methods

#### 3.1 Materials

Different types of CNFs were prepared from commercial bleached birch kraft pulp (BKP) (**Paper I, II & III**). Balsa wood slice (**Paper IV**) was purchased from Xuhong Co. Ltd., Shanghai. The chemicals used in this thesis were purchased from Sigma- MERCK, Aldrich, Macklin, Sinopharm Chemical Reagent Co. Ltd. (Beijing, China), or VWR without any treatment prior to use.

#### 3.2 Preparation methods

##### 3.2.1 Preparation of TEMPO-oxidized CNFs (**Paper I, II**)

The TEMPO-oxidized CNFs were produced following the protocol previously reported.[119] Briefly, 5 grams dried pulp was added into 300 mL water and stirred overnight. Then 80 mg TEMPO reagent and 500 mg NaBr were added into 200 mL water and then mixed with the fiber suspension. The mixture solution pH was adjusted to 10.0 by 0.5 M NaOH. The oxidation reaction started by dropwise adding 30 mL NaClO solution within 30 min. The pH was then kept at 10.5 until the pH became stable. The oxidized fibers were then added in ethanol for precipitation and washed with centrifugation. The TEMPO-oxidized CNFs (0.5 %) were obtained by homogenizing at 600 bar for two cycles and stored at 4.0 °C.

##### 3.2.2 Preparation of AO-CNFs (**Paper III**)

Commercial cellulose pulp (3 g) was first immersed in 2 mL 10 wt%  $C_4H_{12}NCl$  for 5 min at around conditions. Then the pulp was mixed with 70 ml acrylonitrile solution and 2 ml 36% NaOH and stirred for 30 min at ambient conditions ( $25 \pm 2$  °C). The reaction mixture was then washed with deionized water, neutralized with acetic acid (1 wt%), and freeze-dried. Amidoximation was carried out according to the published literature[120].  $NH_2OH \cdot HCl$  (4.17 g, 60.0 mmol) was stirred and dissolved in 45 ml DMF at 45 °C. Then  $Na_2CO_3$  (2.87 g, 27.0 mmol) and NaOH (0.72 g, 18.0 mmol) were added slowly. After stirring for 4 h, cyanoethyl cellulose (1 g) was added and kept for 30 min at 45 °C, and further stirred for 24 h at 65 °C. Finally, 1.43 g  $Na_2CO_3$  and 0.36 g NaOH were added, and the reaction was kept at 65 °C for 24 h. Then, the mixture solution was centrifuged and washed with water to precipitate a white floc. The filtrated precipitate was freeze-dried. The AO-CNF were then dispersed in 0.15 M NaOH and neutralized with deionized water through dialysis.

##### 3.2.3 Preparation of AO-CNF membrane (**Paper III**)

AO-CNF membranes with different thicknesses were obtained by vacuum-assisted filtration of different amounts of AO-CNF dispersions on 200 nm commercial nylon membranes.

### 3.2.4 Preparation of CNF/PEI/Ag NPs aerogel (Paper I)

0.6 wt% CNF suspension (pH 10) was mixed with 25% PEI solution (pH 10) at the weight ratio of 1:1 and stirred for 1 min. Then the CNF/PEI aerogel was prepared by pouring the mixture into a plastic tube and freeze-dried. Then the CNF/PEI aerogel was prepared by freeze-drying. The aerogel was decorated with Ag NPs by adding into 20 mL 10 mM AgNO<sub>3</sub> solutions for 12 h and transferred into 20 mL 15.4 mg L<sup>-1</sup> NaBH<sub>4</sub> for 3 h.

### 3.2.5 Preparation of CNF/PEI/ECH aerogel (Paper II)

20 mL 0.4% CNF (pH 13) suspension was mixed with different amount of 25% PEI solution (pH 12) with various weight ratio (1: 0.5, 1:1, and 1:2) under stirring for 30 min. Then 0.25 mL ECH was added into the mixture under stirring for 30 min and poured into the tube and kept at 60 °C for 2 h to ensure the reaction. The CNF/PEI aerogels with the weight ratio at 1: 0.5, 1:1, and 1:2 were named CPE-0.5, CPE-1, CPE-2, respectively. The samples of CNF: PEI (1:2) without ECH was named CPE-20.

### 3.2.6 Preparation of AO-wood aerogel (Paper IV)

Wood slice (2 g) was immersed in 72 mL acrylonitrile solution, and then 2 mL 10% NaOH was added, and the mixture was stirred 24 h at the ambient environment (25 ± 2 °C). The wood samples were then washed thoroughly with deionized water. The cyanoethylated-wood (AN-wood) was then obtained after freeze-drying. To amidoximate AN-wood into AO-wood, 12 g NH<sub>2</sub>OH·HCl was dissolved in 100 mL water, followed by adding 6.9 g NaOH and stirred at 45 °C for 2h. AN-wood was put in the solution and stirred at 70 °C at different times. The wood was collected, washed, and freeze-dried to prepare AO-wood aerogel.

## 3.3 Characterization methods

### 3.3.1 Carbohydrate analysis (Paper IV)

The chemical composition of the wood samples was analyzed according to National Renewable Energy Laboratory (NREL/TP-510-42618) procedure[121]. In brief, carbohydrate analysis was carried out by grinding the samples into 20-80 mesh, subsequently, the samples were completely hydrolyzed. The content of carbohydrates was determined by High-performance liquid chromatography (HPLC) (Model 1200, Agilent, USA) equipped with a Bio-Rad Aminex HPX-87P column. The lignin content was also calculated by the NREL/TP-510-42618 procedure.

### 3.3.2 Spectrometry and microscopy

FTIR: The Fourier Transform infrared spectroscopy (FTIR) analyses in **Paper I & II** for analyzing the CNF/PEI/Ag NPs and CNF/PEI/ECH samples were carried out with a Thermo Scientific Nicolet iS™ 50, USA at 64 scans from

4000 to 400  $\text{cm}^{-1}$  with a resolution of 4  $\text{cm}^{-1}$ . The FTIR spectra of the AO-CNF and AO-wood were analyzed with a Thermo Fisher Nicolet 6700 FTIR Spectrometer (**Paper III & IV**). The parameters for the analysis were the same as described above. X-ray photoelectron spectroscopy (XPS): Elemental electron binding energy was obtained with an XPS (ESCALab 250Xi, VG Scientific, Britain), with a monochromatized Al K $\alpha$ -radiation at 50 W and 15 kV. (**Paper III & IV**)

Atomic force microscopy (AFM), scanning electron microscopy (SEM), and transmission electron microscopy (TEM): The morphology of AO-CNF was characterized by AFM. In Paper III, the AO-CNF suspension was deposited on a silica wafer and dried in the oven at 70 °C for characterization by Bruker Agilent 5400 (Germany). The SEM of the samples in **Paper I & II** were characterized by SEM LEO Gemini 1530 (Thermo scientific, germany). In **Paper III & IV**, the SEM analyses were done with a JEOL 7401 (Japan). The double-side sticking tape fixed the samples at the accelerating voltage is 2.7 kV. The TEM images were recorded with a Hitachi H-7650 (Japan) with 100 kV accelerating voltage. 5  $\mu\text{L}$  of the diluted samples were dropped on a carbon-supported copper grid and stained by 5  $\mu\text{L}$  0.5 wt% uranyl acetate solution for 15 min. Then the solution was adsorbed, and the samples were air-dried before for the measurement.

### 3.3.3 Elemental analysis (Paper II, III & IV)

The elemental content of the obtained samples was studied by elemental analysis (EA, Vario EL cube elemental analyzer, Elementar Analysensysteme GmbH).

### 3.3.4 Brunauer-Emmett-Teller (BET) (Paper I, II & IV)

The specific surface areas in **Paper I & II** were analyzed and calculated by nitrogen sorption at  $-196\text{ }^{\circ}\text{C}$  through TriStar 3000 (Micromeritics Inc.). The  $\text{N}_2$  physisorption isotherms in Paper IV were obtained from Micromeritics ASAP 2020 at  $-196\text{ }^{\circ}\text{C}$  under a relative vapor pressure of 0.05–1.0. Before the nitrogen adsorption, 0.10 g samples were degassed at 90 °C for 12h.

### 3.3.5 X-ray diffraction (XRD) (Paper III & IV)

X-ray diffractometer (Bruker D8 ADVANCE) was used to analyze the XRD patterns of the samples (**Paper I, III & IV**) with Cu-K $\alpha$  ( $\lambda = 1.5406\text{ \AA}$ ) radiation.

### 3.3.6 Thermal properties (Paper I)

Thermal Gravimetric Analyser (TG) (Q500, TA instruments) was used to analyze the thermal stability of the samples. Before thermal analysis, the samples were kept in a 40 °C vacuum desiccator until completely dried. The analysis was carried out with a heat rate at  $10\text{ }^{\circ}\text{C min}^{-1}$  from around temperature to 900 °C under an  $\text{N}_2$  atmosphere.

### 3.3.7 Zeta-potential (Paper III)

The zeta-potential of the obtained materials was analyzed by a zeta potential analyzer (NanoPlus-2, Micromeritics Co, Ltd., China). All the sample suspensions with 0.1 wt.% were ultrasonicated (VMR, 80W) for 30 min before the measurement.

### 3.3.8 Mechanical properties

The mechanical performance of the samples (**Paper II, III & IV**) was investigated with a universal testing machine. The tensile and compressive tests in **Paper II & IV** were conducted at a strain rate of 2 mm min<sup>-1</sup>. Before the wet mechanical performance test, the samples were immersed in distilled water overnight. Every sample was tested three times.

### 3.3.9 Catalytic reduction performance (Paper I)

To investigate the catalytic reduction performance of the samples, the tests were carried out in dye solutions including NaBH<sub>4</sub> and stirred slightly. UV-Vis spectroscopy was used to record the catalytic process at intervals of 1 min. Briefly, the prepared samples were added into 40 mL, 10 mg L<sup>-1</sup> organic dye solutions and then 10 mL NaBH<sub>4</sub> (50 mM) was added to start the catalytic discoloration process.

To test the continuous flow catalytic performance, 10 mL NaBH<sub>4</sub> (50 mM) and 40 mL dye solution (10 mg L<sup>-1</sup>) passed through the obtained sample. The dye concentration changes after passing through the aerogel were investigated by UV-Vis spectrophotometry. The reduction efficiency was calculated according to the equation:

$$\text{Efficiency (\%)} = 100 * (C_0 - C) / C_0 \quad (1)$$

in which C<sub>0</sub> is the original dye solution concentration, and C is the dye solution concentration after passing through the aerogel. The water transportation of the aerogel was also calculated with the following equation:

$$J = V / (A t) \quad (2)$$

where V is the mixture volume (unit: L), A is the effective area (unit: m<sup>2</sup>) of the samples, and t is the time (unit: h) for the process.

### 3.3.10 Dye adsorption measurements

To investigate the dye adsorption performance of the samples in **Paper II**, 10 mg samples were added into 25 mL MO solutions with stirring at the ambient environment for a certain time. The adsorption process was recorded by a UV-2600 in the 350-700 nm. The adsorption uptake (q<sub>e</sub>) was calculated by the following equation:

$$q_e = V * (C_0 - C_e) / m \quad (3)$$

in which  $q_e$  is the adsorption uptake ( $\text{mg g}^{-1}$ ),  $C_e$  represents the equilibrium dye concentration ( $\text{mg L}^{-1}$ ),  $C_0$  is the original dye concentration ( $\text{mg L}^{-1}$ ),  $V$  is the dye solution volume (L), and  $m$  is the sample weight (g).

To investigate the adsorption kinetics and adsorption isotherms, the prepared samples were carried out in different concentrations of MO solutions, and analyzed according to the following equation:

The Langmuir model:

$$q_e = \frac{b q_{\max} C_e}{1 + b C_e} \quad (4)$$

Where  $C_e$ ,  $q_m$ , and  $b$  present the equilibrium MO concentration, the maximum adsorption capacity ( $\text{mg g}^{-1}$ ), and the Langmuir constant ( $\text{L mg}^{-1}$ ).

The non-linearized Freundlich model:

$$q_e = k_f C_e^{\frac{1}{n_f}} \quad (5)$$

In which  $k_f$  and  $1/n_f$  represent the Freundlich isothermal constants ( $\text{mg g}^{-1}$ ) and intensity of adsorption.

The pH influence on the MO adsorption performance in the range of 2–11 was tested in the  $1000 \text{ mg L}^{-1}$  MO solution. To test the flow behavior, different amounts of MO solution at  $10 \text{ mg L}^{-1}$  were passed through the aerogel by gravity. The regeneration and recyclability of samples were studied by immersing  $10 \text{ mg}$  MO-uptake aerogel in  $0.1 \text{ M NaOH}$  solution. Then the aerogel was neutralized with DI water for another test.

### 3.3.11 Uranium removal performance measurements

Aquatic uranium element removal performance was studied in **Paper III & IV**. Batch experiments of uranyl ions ( $\text{UO}_2^{2+}$ ) adsorption were carried out with  $10 \text{ mL}$  aqueous solution with different concentrations of U (VI) (pH 8). Typically,  $4 \text{ mg}$  samples were mixed with  $10 \text{ mL}$  different concentrations of U (VI) and stirred vigorously for different adsorption times. Then, the U (VI) content before and after adsorption was measured according to the method based on arsenazo III uranium which can coordinate with  $\text{UO}_2^{2+}$ . [122] The adsorbed amount  $q_e$  ( $\text{mg g}^{-1}$ ) at equilibrium was calculated by the equation above (1).

To test the pH effect on the uranium adsorption (**Paper III & IV**), pH values (3–9) of U (VI) solution and adsorbent were equated using  $0.1 \text{ M HCl}$  and  $\text{NaOH}$ . To test the reusability of this adsorbent, the desorption of adsorbed uranium was eluted with a mixture solution of  $1 \text{ M Na}_2\text{CO}_3$  and  $0.1 \text{ M H}_2\text{O}_2$  at around environment temperature ( $25 \pm 2 \text{ }^\circ\text{C}$ ). The elution ratio (%) was also determined by the UV-vis spectrum. The adsorption isotherms were simulated according to the Langmuir and Freundlich isotherm models according to the equation (4) and (5).

Adsorption performance in real seawater: The uranium adsorption performance of the adsorbent was also studied in natural seawater. Generally, 5 mg adsorbent were immersed in 50 L natural seawater collected from the coast of Laoshan Qingdao, Yellow Sea of China, Shandong Province. After soaking for 30 days, the adsorbents were collected and digested under microwave digestion for 1 h, filtered and diluted with deionized water, and inductively coupled plasma–mass spectrometry (ICP-MS) determined the uranium concentration. The adsorption capacity was determined using Equation (3).

Filtration test: AO-CNF membranes with different thicknesses were prepared through vacuum-assisted filtration of different volumes of AO-CNF dispersions on 200 nm nylon filtration membranes (VWR) in **Paper III**. The filtration test (**Paper III & IV**) was carried out on a vacuum VWR filtration device. Water flux ( $F$ ,  $\text{L m}^{-2} \text{ h}^{-1} \text{ bar}^{-1}$ ) was calculated by filtrating 10 mL water passed the membrane according to the equation:

$$F=V/AtP \quad (6)$$

, where  $V$  is the filtered water volume (L),  $A$  is the effective membrane filtration area ( $\text{m}^2$ ),  $t$  is the time (h), and  $P$  is the suction pressure (bar).

## 4. Results and discussion

### 4.1 Overview of the thesis work

The overall work in this thesis aimed to develop novel functional materials from wood-derived materials in water remediation in a new-generation biorefinery concept. As shown in **Figure 4.1**, the wood pulp or native wood can be used as raw materials to prepare CNF suspensions, aerogels, membranes, and wood aerogels through different approaches.



**Figure 4.1.** Overview of the thesis work.

The specific workflow of the thesis is as follows:

- 1) Preparation of robust shape-retaining CNF/PEI/Ag NPs aerogels and testing of the continuous catalytic discoloration towards organic dyes.
- 2) Development of ultralight and porous CNF/PEI aerogels for selective anionic dye adsorption.
- 3) Fabricating AO-CNF and testing of the uranium extraction performance.
- 4) Making anisotropic highly mesoporous AO-wood aerogels for enhanced uranium recovery.

### 4.2 CNF/PEI/Ag NPs aerogels for continuous catalytic discoloration towards organic dyes (Paper I)

Catalytic reduction of organic dyes has been studied widely for dye-contaminated wastewater for the high efficiency and easy processing. In the reduction procedure, noble metal particles were usually chosen as the catalysts for dye discoloration. Ag NPs, one of the most important and common noble metal catalysts, have been developed for many years to catalyze discoloration of dye-contaminated wastewater due to their high catalytic efficiency.[123] However, Ag NPs are easily aggregated in the working process due to their high surface energy, resulting in the decrease of catalytic performance. To date, nanocellulose (CNC, CNF, and BC) have attracted interest as supports for catalysts because of their large specific surface area, chemical stability, good

dispersibility, and low cost. Therefore, the nanocellulose-based aerogel decorated with Ag NPs was prepared in this work, and this novel composite aerogel provides a new way to deal with dye-contaminated wastewater.

#### 4.2.1 Preparation of CNF/PEI/Ag NPs composite aerogel

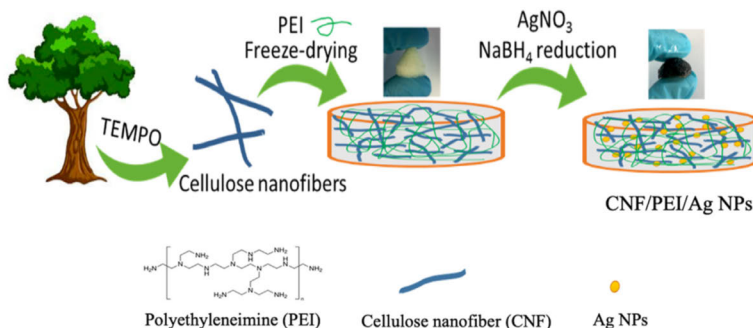


**Figure 4.2.** Scheme of the process for preparing CNF/PEI/Ag NPs aerogel (Copyright by Elsevier, 2020).

As shown in **Figure 4.2**, the CNF/PEI/Ag NPs were prepared via the physical interaction between negatively charged CNFs and positively charged PEI, decorated with Ag NPs. In brief, we firstly produced CNF by TEMPO oxidation, and the CNF mixed with PEI to prepare CNF/PEI aerogel after freeze-drying. The CNF/PEI was then decorated with Ag NPs and the CNF/PEI/Ag NPs samples were finally obtained.

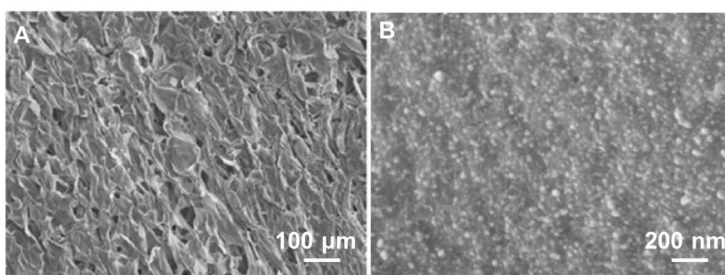


**Figure 4.3.** SEM images of the CNF/PEI/Ag at different magnifications.

The morphology of CNF/PEI/Ag NPs samples was studied by SEM, as is shown in **Figure 4.3**. The sample consisted of micro-sized pores, and small Ag NPs were decorated on the pore walls in the cross-section images. The large number of micro-pores is vital for the process of the catalytic reduction reaction.

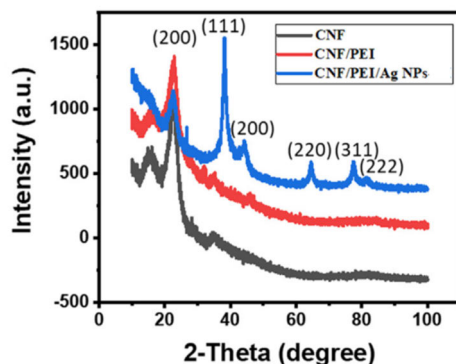


**Figure 4.4.** XRD profiles of the CNF, CNF/PEI, CNF/PEI/Ag NPs samples.

The crystalline structures of the samples were studied by X-ray diffraction from  $10^\circ$  to  $100^\circ$ , as shown in **Figure 4.4**. The presence of Ag NPs was identified by the diffraction peaks at  $2\theta=38.0^\circ$ ,  $44.1^\circ$ ,  $64.4^\circ$ ,  $77.4^\circ$ , and  $81.5^\circ$  corresponded to the diffraction of the (1 1 1), (2 0 0), (2 2 0), (3 1 1), and (2 2 2). [124, 125] The results showed that the Ag NPs were successfully prepared on the samples micropore wall surface and the crystallinity was face-centered cubic (fcc) structure. In addition, the diffraction peaks at  $2\theta = 22.5^\circ$  were attributed to the (2 0 0) lattice planes of cellulose I, indicating that the crystalline structure of CNF did not change during the making process.

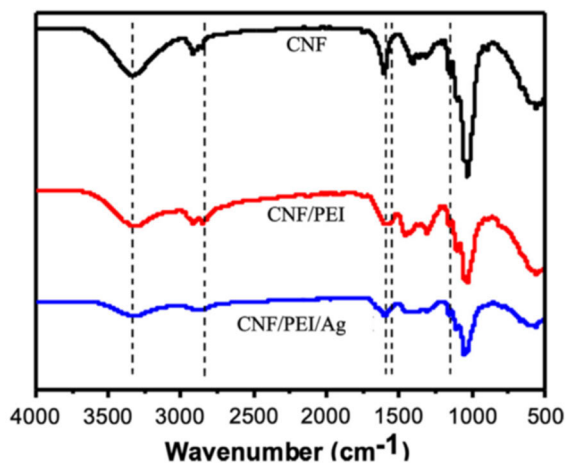


**Figure 4.5.** FTIR spectra of obtained CNF, CNF/PEI, and CNF/PEI/Ag samples (Copyright by Elsevier, 2020).

The FTIR spectra of different samples are illustrated in **Figure 4.5**. The typical characteristic peaks of CNF at  $3334$  and  $1601\text{ cm}^{-1}$  were corresponded to  $\text{-OH}$  and  $\text{-C=O}$  stretching vibration. [126-128] The characteristic spectra for the CNF/PEI at  $2842\text{ cm}^{-1}$  was related to  $\text{-CH}_2$ , and  $1556\text{ cm}^{-1}$ , and  $1166\text{ cm}^{-1}$  were attributed to  $\text{-NH}_2$ , and C-C skeleton vibration, respectively. [129] As can be seen, the peak of  $\text{-OH}$  ( $3334\text{ cm}^{-1}$ ) became weaker for the sample CNF/PEI/Ag.

What is more, the intensity for the  $\text{-C=O}$  at  $1601\text{ cm}^{-1}$  also decreased. The results above indicated that numerous hydrogen bonds and electrostatic interactions exist among the  $\text{-OH}$ ,  $\text{-NH}_2$ ,  $\text{-COOH}$ , and Ag NPs. Meanwhile, the peak for the CNF/PEI/Ag at  $1556\text{ cm}^{-1}$  ( $\text{-NH}_2$ ) disappeared, indicating the existence of interactions between  $\text{-NH}_2$  and Ag NPs.

#### 4.2.2 Mechanical stability and shape-recovery in water

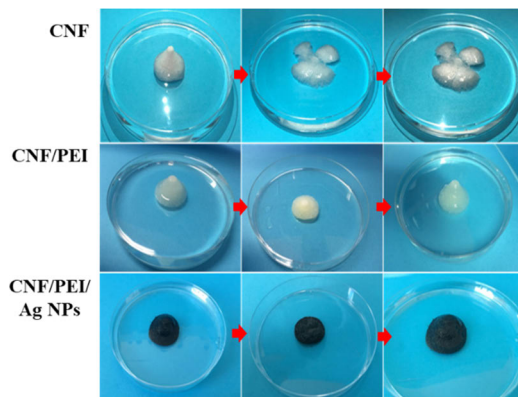


**Figure 4.6.** Mechanical performance and shape-recovery in the water of CNF, CNF/PEI and CNF/PEI/Ag NPs aerogel.

Generally, the wet stability of cellulose-based materials is weak because of their hydrophilic nature. As shown in **Figure 4.6**, the CNF aerogel was easy to be broken by the compressing force. However, the CNF/PEI sample presented high water resistance and shape memory in water. The excellent water resistance performance for the CNF/ PEI aerogel was mainly due to ionic bonds and hydrogen bond interaction between amine groups and carboxyl groups.[130] After introducing Ag NPs into the samples, water-resistance and shape memory performance did not change, which is important for CNF/PEI/ Ag NPs for wastewater treatment.

### 4.2.3 Catalytic discoloration of CNF/PEI/Ag NPs for MB and CR

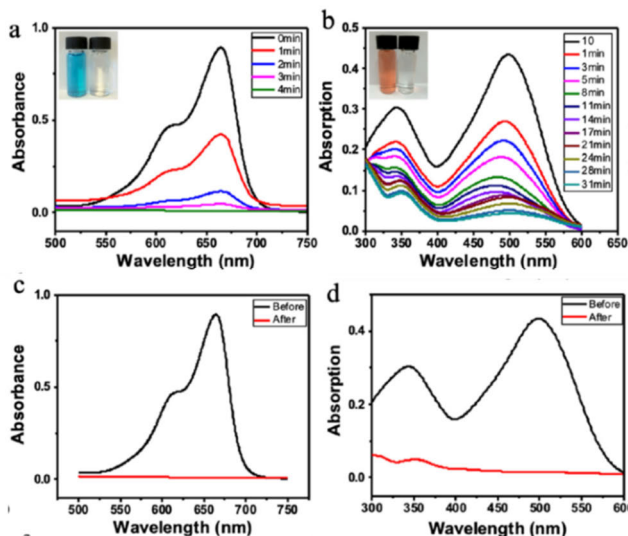


**Figure 4.7.** The discoloration performance for Methylene blue (MB) (a) and Congo red (CR) (b). The discoloration performance of the MB (c) and CR (d) solutions.

In this work, model cationic (MB) and anionic (MO) dyes were chosen for studying the discoloration performance of the obtained samples. The reduction process was recorded by UV-vis spectroscopy. **Figure 4.7a** shows the catalytic process of the sample towards the MB solution. The MB absorption peak decreased as time moves on and disappeared around 4 min, in which the treatment efficiency was high, being up to 96%. In addition, the catalytic process towards the CR solution was further studied in **Figure 4.7b**. The typical absorption peak at 498 nm decreased gradually and disappeared within 21 min. As can be seen, the discoloration efficiency of CR is much lower than that of MB under these conditions because of the different chemical structures between MB and CR.

The continuous flow discoloration efficiency of the samples was also investigated (**Figure 4.7c** and **Figure 4.7d**). The treatment performance towards the MB solution was recorded by UV-Vis spectroscopy. The typical peaks of MB or CR almost disappeared after passing through the sample, and the reduction efficiency for MB and CR reached 99.2% and 96.4%, respectively. In addition, the samples exhibited fast water transportation, which reached  $5 \times 10^4 \text{ L} \cdot \text{m}^{-2} \text{ h}^{-1}$ .

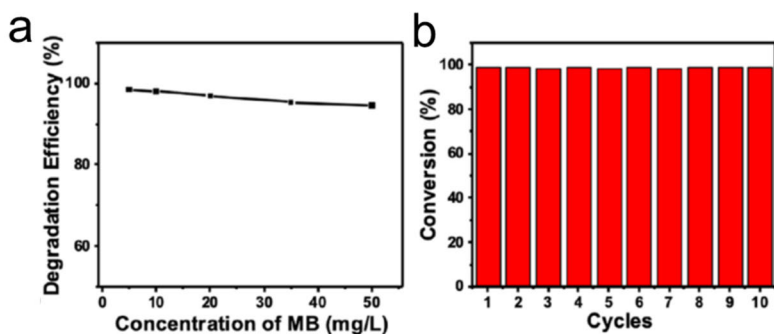


**Figure 4.8.** (a) The treatment performance of CNF/PEI/ Ag NPs with different MB concentrations solution. (b) The treatment performance of MB during 10 times continuous catalytic reduction process.

The influence of the concentration of the MB solutions on the degradation efficiency of the membrane is shown in **Figure 4.8a**. The sample presented high discoloration efficiency, and only with a slight decrease with increasing the MB concentration from 5 mg L<sup>-1</sup> to 50 mg L<sup>-1</sup>. **Figure 4.8b** illustrates that the treatment efficiency was still above 98% even after 10 times catalytic processes. Hence the samples possess excellent discoloration performance and reusability, which is important for a long time test of the aerogel.

### 4.3 Dual cross-linked CNF/PEI composites for selectively removing anionic dye (Paper II)

In recent years, cellulose, the most common natural polymer, has been studied widely to prepare adsorbents to treat organic dyes contaminated wastewater.[131] Therefore, a strategy to develop porous CNF/PEI composite aerogel with good structural stability was proposed. The fabrication process of CNF/PEI composite aerogels is illustrated in **Figure 4.9**. CNF suspensions were firstly mixed with PEI solution and then crosslinked with ECH. Then the ultralight and porous CNF/PEI aerogel was prepared through freeze-drying and further used for organic dye adsorption.

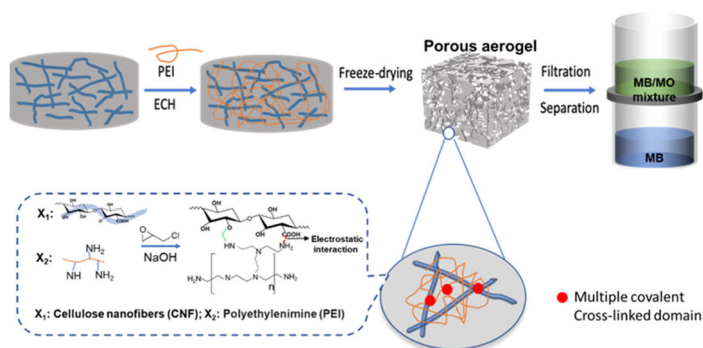


**Figure 4.9.** Scheme of the process for preparing CNF/PEI samples and their selective removal performance for dye mixtures (Copyright by Elsevier, 2022).

### 4.3.1 Morphology and properties of the CNF/PEI aerogels

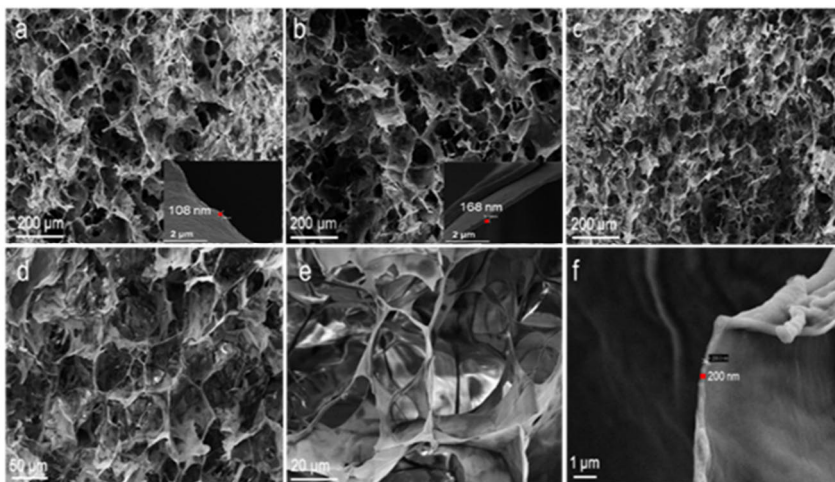


**Figure 4.10.** SEM images for the different CNF/PEI samples: (a) CPE-0.5; (b) CPE-1; (c), (d), (e), (f) CPE-2.

The morphology of the CNF/PEI aerogels with different PEI:CNF weight ratios were studied by SEM (**Figure 4.10**). The different CNF/PEI samples all showed internal nano- and microstructures, and the thickness of the pore wall increased from 108 to 200 nm, and the density increased from 6.75 to 13.02 cm<sup>-3</sup>. In addition, the porosity was above 98%, and the median pore diameter increased from 49498 to 69506 nm, which is vital for the mass transfer process and water transportation (**Table 4.1**).

**Table 4.1.** Properties of the sample CPE-0.5, CPE-1, and CPE-2.

Sample	Porosity (%)	Density (mg cm <sup>-3</sup> )	BET SSA (m <sup>2</sup> g <sup>-1</sup> )	Median pore diameter (nm)	Water uptake (g g <sup>-1</sup> )	Pure water flux (LMH)
CPE-0.5	98.64	6.75	3.1±0.2	49489	71.13	3529
CPE-1	98.58	9.03	3.1±0.1	59936	62.54	3787
CPE-2	98.21	13.02	3.0±0.1	69506	54.65	3950

### 4.3.2 Shape recovery, water stability, and mechanical performance

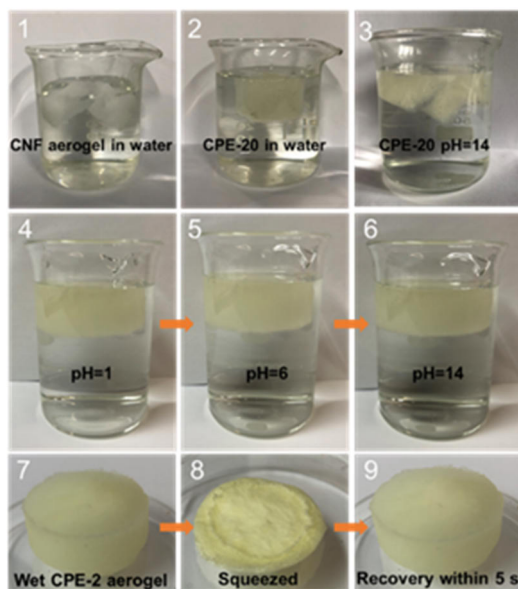


**Figure 4.11.** Water resistance and shape memory: CNF (1), CPE-20 (2), and CPE-20 (3). Water resistance of CPE-2 in different pH water solutions (4, 5, 6); CPE-2 aerogel can be squeezed and rapidly recovered in water (7, 8, 9).

The water-resistance and shape recovery of the aerogels are presented in **Figure 4.11**. For the original CNF aerogel, the structure was destroyed immediately after adding in water, and CPE-20 showed excellent water stability and was destroyed at pH 14 (**Figure 4.11 1, 2, and 3**). However, the CPE-2 sample presented high water resistance in different water conditions without any structure deterioration (**Figure 4.11 4, 5, and 6**), which is vital for the sample working in different environments and regeneration. In addition, CPE-2 also presented high water uptake performance and shape memory. CPE-2 can absorb more than 50 times of water compared with its weight, and more than 90% of the absorbed water could be squeezed out easily. Once the squeezed CPE-2 is immersed in the water again, it can return to its original shape by absorbing the water immediately (**Figure 4.11 7, 8, and 9**), indicating the superior water-activated shape recovery performance.

### 4.3.3 Adsorption and filtration performance in batch

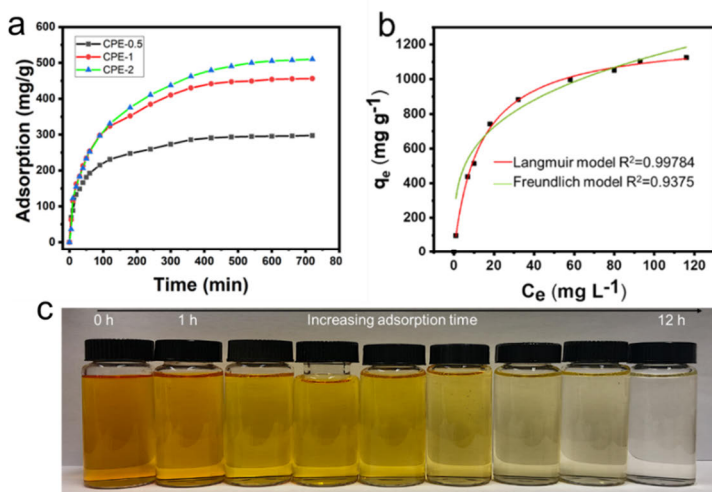


**Figure 4.12.** a) The MO adsorption process of CNF/PEI samples (with the weight ratio at 1: 0.5, 1:1, and 1:2 named CPE-0.5, CPE-1, CPE-2) as time moves on, b) The Langmuir and Freundlich model of the CPE-2 sample for MO adsorption at pH 6, and c) photographs of the MO solution changes with different adsorption time.

The adsorption performance of the CNF/PEI samples was studied, in which MO was chosen as a model compound. **Figure 4.12a** presents the time-dependent adsorption amount, and the adsorption rate decreased with increasing adsorption time. The uptake ability of the samples increased from 297.5 mg g<sup>-1</sup> to 507.5 mg g<sup>-1</sup> with increasing the weight ratio of CNF:PEI from 0.5:1 to 1:2. To further study the adsorption process, the adsorption kinetics and isotherms were also studied. As shown in **Figure 4.12b**, the data revealed that the adsorption process was monolayer Langmuir adsorption. **Figure 4.12c** presents the digital photographs of MO solutions after the CPE-2 sample was added. The MO solution color became light as time moves on and eventually became nearly transparent after 12h.

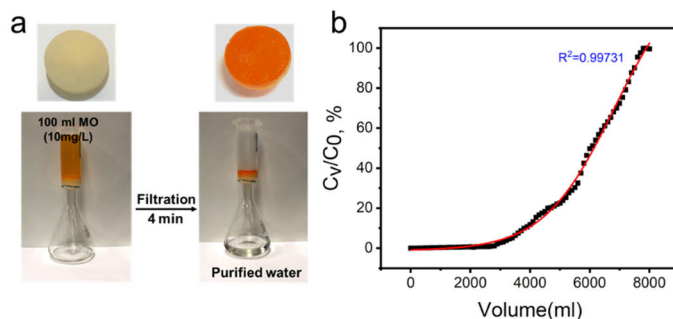


**Figure 4.13.** (a) Filtration adsorption and desorption performance of CPE-2 towards MO, (c) The breakthrough curve of the volume of permeation solution.

The filtration performance was also tested by passing through the CPE-2 sample to realize rapid dye removal through continuous flow. **Figure 4.13a** presents that the MO solution became colorless after passing CPE-2 aerogel with high water transport, up to  $3950 \text{ L m}^{-2} \text{ h}^{-1}$  driven by gravity. **Figure 4.13b** shows the breakthrough curve of the volume of permeation solution. As can be seen, the MO concentration in the outlet increased slowly and eventually close to the initial concentration at 8000 mL. At this time, the capacity of the sample reached  $960 \text{ mg g}^{-1}$ , which was higher than most of the recently reported data.[19, 113, 132-136]

#### 4.3.4 Regeneration and recyclability

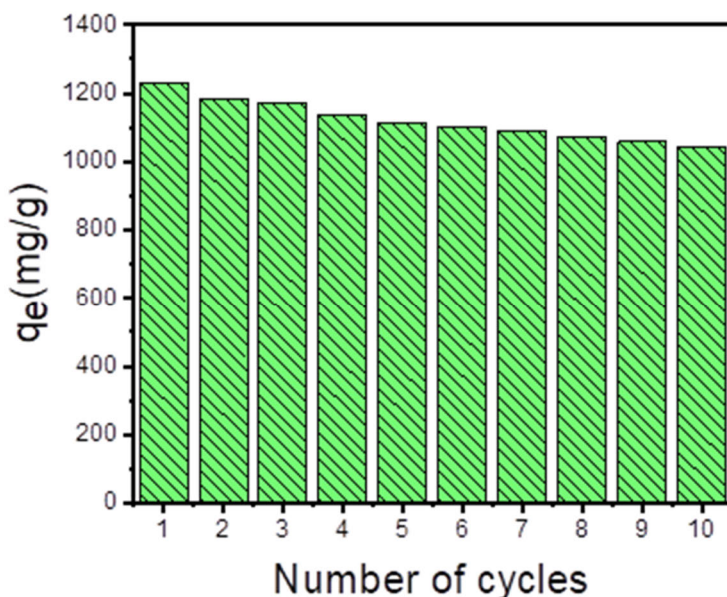


**Figure 4.14.** 10 cycles of the adsorption-desorption of CPE-2 for MO during 10 cycles of regeneration using 0.1M NaOH solution for the adsorption-desorption of MO.

To investigate the regeneration and recyclability performance of CPE-2, a certain amount of CPE-2 was added into 25 mL MO solution ( $1000 \text{ mg L}^{-1}$ ) under continuous stirring at around conditions. Then the adsorbents were taken out and transferred into 0.1 M NaOH solution under mild stirring for regeneration (5 min). The regenerated samples were further washed with water and then used for the following test. As can be seen in **Figure 4.14**, the CPE-2 remained a highly stable adsorption capacity, which can still maintain  $1044.3 \text{ mg g}^{-1}$  after 10 cycles.

### 4.3.5 Selective adsorption and separation

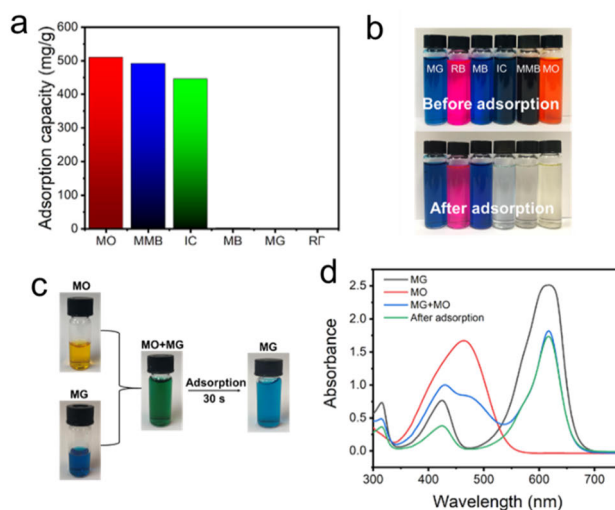


**Figure 4.15.** a) The uptake of the CPE-2 for different dyes; b) The photograph of the CPE-2 for removal of different dyes; c) photographs of CPE-2 for selective removing MO and (d) the related UV-vis spectra.

The selective organic dye removal performance of the CPE-2 is presented in **Figure 4.15a**. The CPE-2 sample showed high adsorption performance for anionic dyes (MO, 512 mg g<sup>-1</sup>; Methylthymol blue (MMB), 496 mg g<sup>-1</sup>; Indigo carmine (IC), 456 mg g<sup>-1</sup>). However, the removal performance of CPE-2 towards cationic dyes (MB, Malachite green (MG), Rhodamine B (RB)) was low to 0. **Figure 4.15b** showed that the color of the anionic dye solutions became almost colorless after adsorption, and the color of cationic dye solutions didn't change obviously. The selective adsorption was also studied in the mixture of anionic and cationic dyes. **Figure 4.15c** presented that the mixed MO/MG solution was dark green, and when CPE-2 was added into the mixed dye solution after recycled squeeze and released for 30 s, the mixture changed from dark green to blue (MG). This phenomenon was also investigated by the UV-vis spectra at different stages, as shown in **Figure 4.15d**. The adsorption peak of MO disappeared after adsorption. In contrast, the absorbance peak of MG remains stable, indicating the selective removal of MO in the adsorption process.

## 4.4 Preparation of AO-CNF membrane for uranium adsorption

### (Paper III)

Extracting the aquatic uranium element has been studied worldwide for its great significance for green energy acquirement and water environmental remediation.[137, 138] Intensive research endeavours have primarily focused on improving the adsorption capacity, selectivity, and dynamics of adsorbents, which have been developed as diverse as inorganic materials (e.g., clay and

silica),[139, 140] organic polymers (e.g., resins and cellulose),[141, 142] carbon materials (e.g., activated carbon and graphene)[143, 144] and metal/covalent-organic frameworks (i.e., MOF/COF).[145, 146] CNFs as an emerging nanomaterial have been studied widely in water remediation. Therefore, developing CNFs with special functional groups can be used for uranium extraction.

#### 4.4.1 Synthesis of AO-CNF

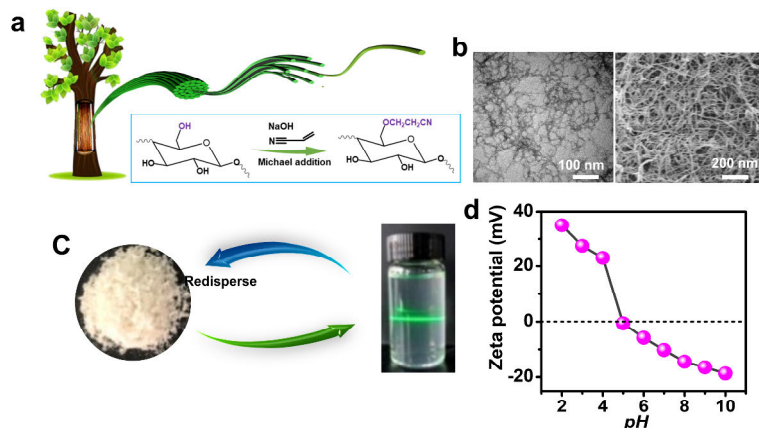


**Figure 4.16.** a) Extraction procedure of AO-CNF from commercial softwood pulp; b) TEM and SEM images of AO-CNF; c) Redisperisability of freeze-dried AO-CNF; d) Zeta potential of AO-CNF at different pH values (2–10).

As shown in **Figure 4.16a**, cyanoethyl cellulose was first produced via the Michael addition between cellulosic hydroxyls and acrylonitrile.[147] Then, the AO-CNF was prepared in DMF dispersion through the addition reaction of C≡N with hydroxylamine. The nanofibrous structure was confirmed by TEM and SEM observation (**Figure 4.16b**). Furthermore, AO-CNF presented redisperisability in water (**Figure 4.16c**). To be noted, at pH 8 (the approximate pH value of natural seawater) AO-CNF exhibited a Zeta potential of ~-15 mV in aqueous suspension (**Figure 4.16d**), and their freeze-dried powder could be redispersed in aqueous suspension with obvious Tyndall effect (**Figure 4.16c**).

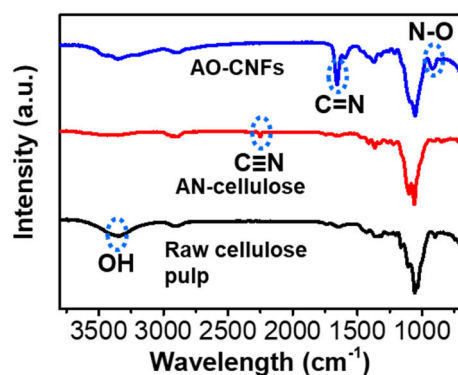


**Figure 4.17.** FTIR spectra of cellulose pulp, cyanoethylated cellulose, and AO-CNF.

The FTIR spectra of native cellulose pulp, cyanoethylated cellulose, and AO-CNF were illustrated in **Figure 4.17**. As the reaction proceeded, an obvious FT-IR absorption band at  $\sim 2252\text{ cm}^{-1}$ , attributed to the characteristic stretching vibration of the  $\text{C}\equiv\text{N}$  group,[148] emerged while the  $-\text{OH}$  peak at  $3350\text{ cm}^{-1}$  decreased dramatically. Both of these confirmed the successful introduction of a large number of cyanoethyl groups. After amidoximation, specific FT-IR peaks of  $\text{C}=\text{N}$  at  $1655\text{ cm}^{-1}$  and  $\text{N}-\text{O}$  at  $924\text{ cm}^{-1}$  from amidoxime groups were observed gradually. Meanwhile, the specific peak of  $\text{C}\equiv\text{N}$  group at  $\sim 2252\text{ cm}^{-1}$  had disappeared, verifying the complete amidoximation.

#### 4.4.2 Adsorption of uranium ions

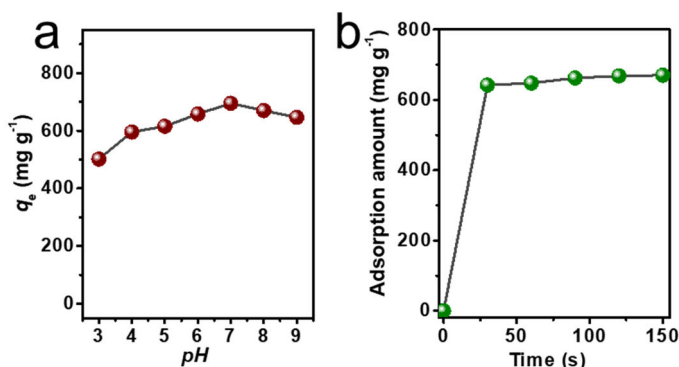


**Figure 4.18.** a) Effect of pH value on the U (VI) ( $500\text{ mg L}^{-1}$ ) adsorption for AO-CNFs; b) The kinetics of U (VI) adsorption from aqueous solution ( $500\text{ mg L}^{-1}$ ), at  $\text{pH}=8$ .

As shown in **Figure 4.18a**, the AO-CNF could reach a measured uptake capacity ( $\sim 665\text{ mg g}^{-1}$ ) in uranyl-spiked water ( $\text{pH} \sim 8$ ; initial U (VI) concentration  $C_0 \sim 500\text{ mg L}^{-1}$ ). Although there is an optimal pH value of 7, this unique type of biological nanofibrils had considerable capacities  $>500\text{ mg g}^{-1}$  in a wide pH range of 3–9, capable of extracting uranium from seawater and

nuclear wastewater with harsh pH conditions. In addition, these biological nanofibrils exhibited high adsorption kinetics, (**Figure 4.18b**). For example, the nanofibrous adsorbent could accomplish ultra-fast adsorption equilibrium within 200 s (sonication time included) with the concentration of U (VI)-spiked water at 500 ppm, which are comparable or superior to the reported U (VI) adsorbents.[140, 145, 149-154]

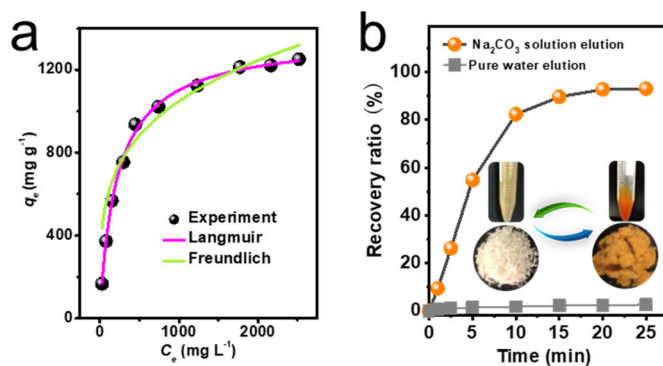


**Figure 4.19.** a) Langmuir and Freundlich model to fit the data (pH=8) with different uranium concentrations; b) U (VI) desorption kinetics of the AO-CNF in the elution solution.

Langmuir and Freundlich models were further carried out to study the adsorption process and mechanism (**Figure 4.19a**). The data presents that the adsorption behaviour was better fitted to the Langmuir model than the Freundlich model indicating that the adsorption process following monolayer adsorption. A maximum equilibrium adsorption capacity ( $q_m$ ) of near 1327 mg g<sup>-1</sup> could be achieved (pH ~8), which should be attributed to the high surface area and large amidoxime groups of these biological nanofibrils. And then, the uranium-saturated nanofibrils could be regenerated by soaking within eluent (1 M Na<sub>2</sub>CO<sub>3</sub> with 0.1 M H<sub>2</sub>O<sub>2</sub>; 5 mL for 4 mg saturated nanofibrils). The results presents that most of the adsorbed uranium (>93%) of could be desorbed within 25 min due to the formation of a highly stable uranyl-peroxo-carbonato complex in carbonate-H<sub>2</sub>O<sub>2</sub> solution[155] (**Figure 4.19b**). The regenerated nanofibrils returned to white color and they can also be dispersed in the water again (**Figure 4.19b**).

#### 4.4.3 Adsorption mechanism

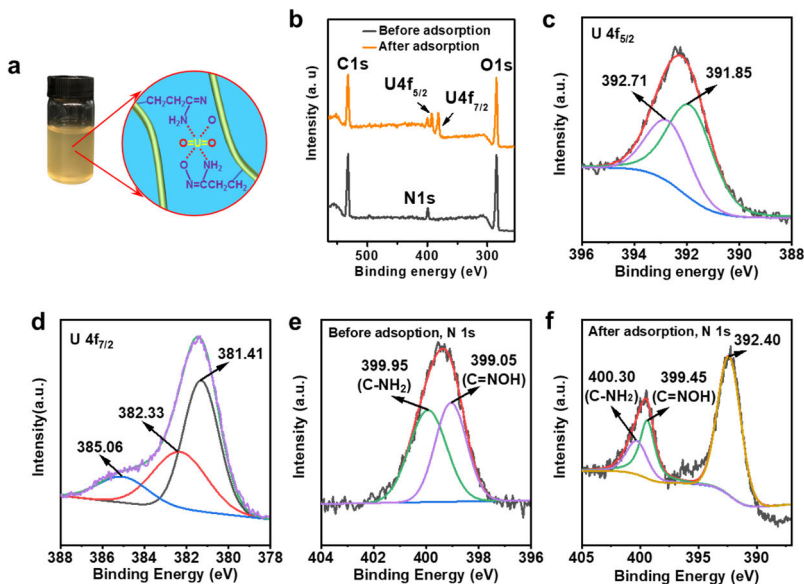


**Figure 4.20.** a) Adsorption mechanism of uranyl ions on the AO-CNF. b) The XPS spectra of the AO-CNFs before and after U (VI) adsorption. High-resolution XPS spectra of the two U4f peaks of the U-uptake AO-CNF (c and d). XPS spectra and high-resolution spectra (N 1s) of the AO-CNF (e) and the uranium loaded AO-CNF (f).

It is vital to investigate the mechanism of the interaction between uranium ions and AO-CNFs. **Figure 4.20a** reveals the proposed chelating mechanism of uranium ions with amidoxime groups. XPS spectra also supported the mechanism, and the uranium uptake process was supported by the peaks of U4f (U4f<sub>5/2</sub>: 392.8 eV and U4f<sub>7/2</sub>: 381.6 eV) of the uranyl ion (**Figure 4.20b**). The high-resolution XPS spectra of the U-uptake AO-CNFs (**Figure 4.20c** and **Figure 4.20d**) further verify the adsorption of uranyl ions on the AO-CNF. In **Figure 4.20c** and **Figure 4.20d**, before U(VI) adsorption, the N 1s peak of AO-CNF was divided into two peaks at 399.95 eV and 399.05 eV. They were attributed to the C-NH<sub>2</sub> and C=NOH.[156, 157] After adsorption of U(VI), the peak at 400.30 eV was assigned for NH<sub>2</sub>, the peak at 399.45 eV was attributed to NOH and the peak at 392.40 eV belonged to C=NOH formed by complexation of U(VI) with oxime. The peaks intensity decreased and the binding energy increased after adsorption due to the interaction between nitrogen-containing functional groups like NH<sub>2</sub> and C=NOH, and uranium ions.[140]

#### 4.4.4 Filtration performance of the AO-CNF membrane

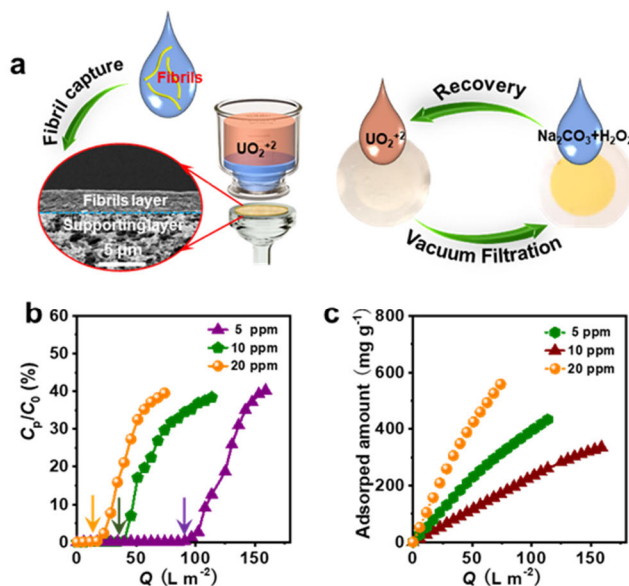


**Figure 4.21.** a) Schematic representation of U (VI) purification by AO-CNF membrane. b) Influence of U (VI) concentration on the breakthrough profiles for U (VI) adsorption in the membranes. c) The calculated adsorbed amount of uranium according to the breakthrough profiles with different U (VI) concentrations.

The large and fast absorption of AO-CNF enables continuous flow uranium removal of their membranes (**Figure 4.21a**). Due to excellent dispersibility and high aspect ratio, AO-CNF could serve as a building unit to construct nanofibrous membranes via vacuum filtration. In the case of a 2.5  $\mu\text{m}$  thick membrane, it could afford a high-water transport ( $\sim 48 \text{ L m}^{-2} \text{ h}^{-1}$ ), an efficient filtration efficiency (99%), and the uranium ions can pass through the membrane completely from its 5-ppm solution with 100  $\text{L m}^{-2}$  permeation (**Figure 4.21b**). The dynamic adsorption capacity was calculated as  $\sim 335$ , 433, and 559  $\text{g g}^{-1}$  for 5, 10, and 20 ppm solution, respectively (**Figure 4.21c**).

## 4.5 Amidoximated wood aerogel for uranium recovery (Paper IV)

### 4.5.1 Preparation of amidoximated wood aerogel

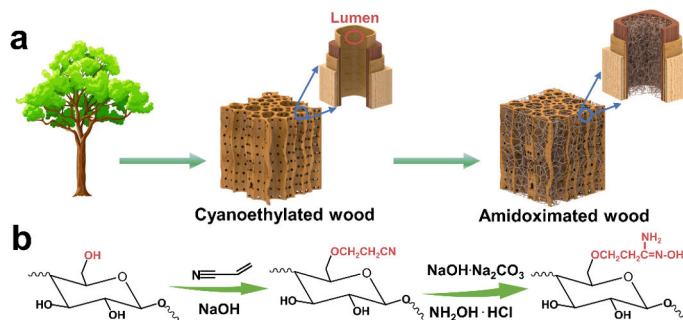


**Figure 4.22.** a) A schematic process for the preparation of AO-wood aerogel. b) Schematic to illustrate the synthetic pathway to produce the AO-wood aerogel.

Balsa wood was firstly used as the starting material to fabricate highly mesoporous aerogels for the efficient removal of uranium ions from seawater or wastewater. As shown in **Figure 4.22a**, natural wood possesses many vertically aligned channels (tens of micrometers) and numerous pits (several micrometers) that decorate the inner surface of the long, curved vessel channels for the transportation of water and nutrients.[158, 159] The multi-channelled structure can endow the native wood as an ideal substrate for developing a new-generation membrane. To fabricate the wood membrane with a hierarchical structure, two steps of chemical modifications were applied to functionalize the natural wood. First, natural wood was cyanoethylated Michael addition between cellulosic hydroxyls and acrylonitrile through alkali-catalyzed reaction.[160] Then AO-wood was obtained through the addition reaction of  $C\equiv N$  with hydroxylamine (**Figure 4.22a** and **Figure 4.22b**).[149]

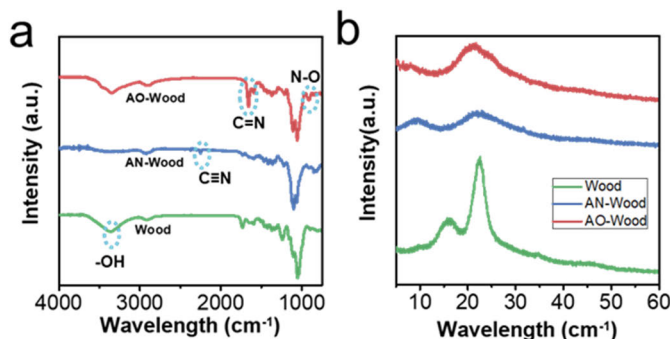


**Figure 4.23.** a) FT-IR spectra of the wood, AN-wood, and AO-wood. b) XRD spectra of wood, AN-wood, and AO-wood.

The group changes were also investigated by FTIR, as well as XPS spectra. The obvious absorption peak at  $\sim 2252\text{ cm}^{-1}$  was assigned to the characteristic

stretching vibration of the C≡N group,<sup>[148]</sup> while the -OH peak at 3350 cm<sup>-1</sup> decreased dramatically, both of which indicated the successful introduction of cyanoethyl groups (**Figure 4.23a**). The content of cyanoethyl groups was as high as 7.34 mmol g<sup>-1</sup>, determined from the elemental analyzer (**Table 4.2**). After amidoximation, the peaks at 2252 cm<sup>-1</sup> disappeared completely while new peaks at 1654 cm<sup>-1</sup> and 992 cm<sup>-1</sup> emerged due to the C=N stretching vibration and N–O stretching vibration, respectively. **Table 4.2** showed the content of the amidoxime group increased with increasing the amidoximation time and was high to 5.61 mmol g<sup>-1</sup> with 15 h. As shown in the XRD patterns (**Figure 4.23b**), upon cyanoethylation typical diffraction peaks at 2θ = 16.2° and 22.7°, attributed to (110) and (200) planes of I-type cellulose crystal[161], observably decreased, implying the possible decrystallization of original crystalline regions. The new diffraction peaks appeared at 9.5 and 21.7°, which is attributed to the regularity of cyanoethylated cellulose polymer chains.[162] The peak at 9.5° disappeared after amidoximation, indicating the cyanoethyl groups were hydrolyzed into the amidoxime group completely.

**Table 4.2.** C, N, and H element content evaluated by elemental analysis and the cyanoethyl groups and amidoxime groups with different hydrolysis times.

Sample	C content (wt%)	N content (wt%)	H content (wt%)	Cyanoethyl (mmol g <sup>-1</sup> )	Amidoxime (mmol g <sup>-1</sup> )
AN-Wood	53.10	10.28	5.10	7.34	-
AO-wood-1h	51.34	11.29	6.11	-	4.03
AO-Wood-3h	46.62	12.45	7.13	-	4.45
AO-Wood-6h	43.18	13.89	6.12	-	4.96
AO-Wood-12h	45.30	15.56	7.33	-	5.56
AO-Wood-15h	42.44	15.72	7.01	-	5.61

#### 4.5.2 Properties of the AO-wood aerogel

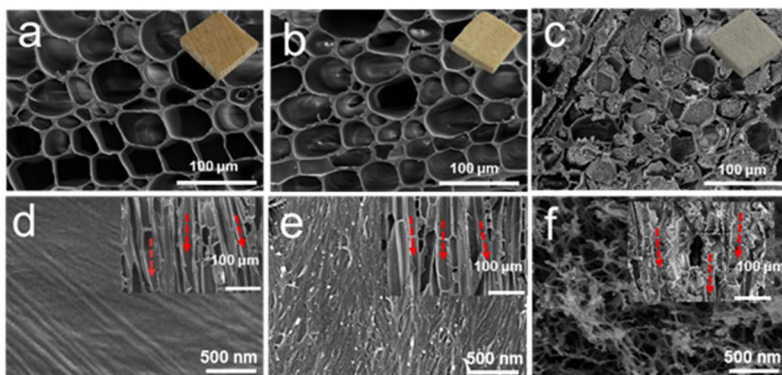


**Figure 4.24.** Photograph and images of the cross-section of native wood (a), AN-wood (b), and AO-wood (c). SEM images of the longitudinal section at different magnifications of native wood (d), AN-wood (e), and AO-wood (f).

The morphology changes of the wood samples were investigated by SEM to show the influence of the two-step chemical process. As shown in **Figure 4.24a** and **Figure 4.24d**, natural wood possesses many vertically aligned channels. Higher magnification SEM images revealed the arrangement of intact cellulose microfibrils on the secondary wall surface. **Figure 4.24b** and **Figure 4.24e** presents that the structure of the AN-wood cell wall became loose compared with native wood, and then a large number of cellulose nanofibrils were formed in the channels by amidoximation **Figure 4.24c** and **Figure 4.24f**. During the procedure, the color of the native wood was changed from yellowish to white, indicating that part of lignin with its chromophores was removed.

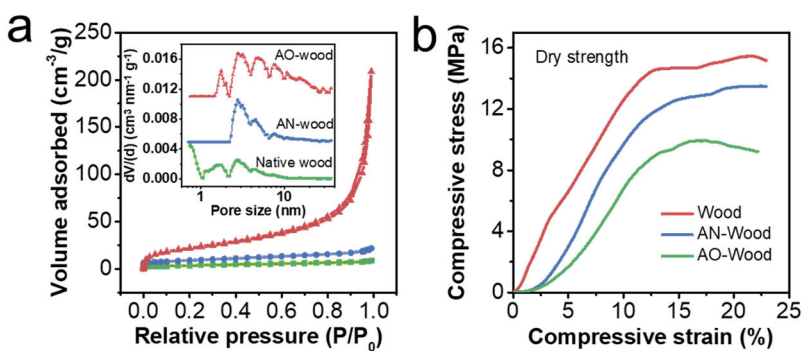


**Figure 4.25.** a)  $N_2$  adsorption-desorption isotherms and pore size distribution derived from  $N_2$  adsorption of the native wood, AN-wood, and AO-wood. b) Compressive stress-strain curves of native wood, AN-wood, and AO-wood at 50% RH.

The  $N_2$  adsorption-desorption isotherms and pore size distribution were investigated by BET measurements through the physisorption of nitrogen ( $N_2$ ). The surface area of cyanoethylated wood is  $31.1 \text{ m}^2 \text{ g}^{-1}$ , while native wood exhibited  $12.7 \text{ m}^2 \text{ g}^{-1}$ . However, the AO-wood showed a high surface area with

78.9 m<sup>2</sup> g<sup>-1</sup>, which is over 6 times compared with that of native wood. The N<sub>2</sub> adsorption/desorption performance of AO-wood is much higher than that of native balsa wood because of the high specific surface area of pores in the cell walls. The above results proved that a hierarchically structured anisotropic aerogel with a high BET surface area is obtained.

**Figure 4.25b** showed the compressive stress-strain curves of the wood sample in growing directions at 50% RH. The Young's modulus of each specimen was 164, 98, and 53 MPa for native wood, AN-wood, and AO-wood, respectively. The structure of native wood starts to collapse at 14.7 MPa, in agreement with previously reported works.[92] The yield stress for AN-wood and AO-wood is 12.8 and 9.98 MPa, respectively. The deterioration of the mechanical performance was mainly due to the defects generated from the partial removal of lignin and hemicellulose. These values were still higher compared to other cellulose composites reported in the literature.[93, 163-174]

#### 4.5.3 Adsorption performance of the AO-wood aerogels for uranium extraction

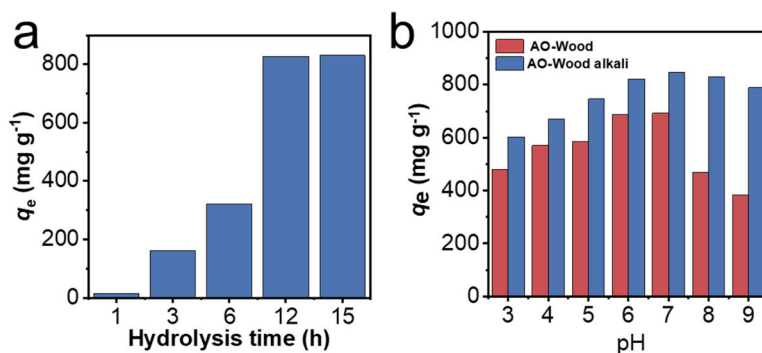


**Figure 4.26.** a) Adsorption capacity of the AO-wood samples at different hydrolysis times. b) Adsorption capacity of AO-wood and AO-wood treated with 20 mM NaOH for 5 min at 50 °C at pH 3–9.

The adsorption performance of adsorbents was mainly determined by the amount of the exposed active adsorption sites. **Figure 4.26a** presents that the adsorption capacity of the AO-wood increased with increasing the hydrolysis time, and the adsorption capacity of the sample with 15 h treatment was the highest (831.3 mg g<sup>-1</sup>) with the initial uranium concentration (500 mg L<sup>-1</sup>) at pH 8. To determine the optimal pH, the uranium adsorption performance of AO-wood was carried out with a pH ranging from 3 to 9. The result revealed that the maximum uranium uptake capacity was achieved at pH 7 (**Figure 4.26b**). The significant decrease of the uranium uptake ability in high and low pH values might result from the interaction between AO-wood and the formed different uranyl species by electrostatic repulsion.[175] In addition, the adsorption capacity of AO-wood was significantly enhanced by alkali treatment due to the deprotonation and conversion of a portion of the amidoxime group into carboxylate resulting in the increase of the hydrophilicity of the adsorbent.[149, 176] The uranium adsorption capacity of AO-wood presented a 22.25%

increase after being treated by 20 mmol NaOH for 5 min at 50 °C compared with that of non-treated AO-wood. Therefore, the alkali-treated AO-wood was studied in the following tests.

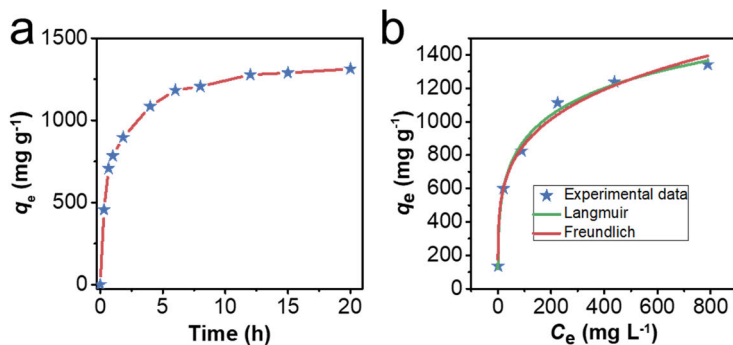


**Figure 4.27.** a) Adsorption kinetics.  $C_0=1500 \text{ mg L}^{-1}$ . b) Langmuir and Freundlich model ( $\text{pH}=8$ ).

To investigate the adsorption mechanism of AO-wood, the sorption kinetics experiments were carried out with the initial uranium concentration of  $1500 \text{ mg g}^{-1}$  at pH 8. The result showed that U (VI) is adsorbed with the extension of time and adsorption equilibrium was achieved around 12 h with the saturation uptake capacity of  $1277.5 \text{ mg g}^{-1}$  (**Figure 4.27a**). The adsorption behavior was then studied by the pseudo-first-order and pseudo-second-order (**Figure 4.27b**) and the experimental data were well fitted with the Pseudo second-order kinetic model ( $R^2 > 0.9977$ ), implying that adsorption of uranium by AO-wood mainly depended on chemisorption. The adsorption performance was further studied by Langmuir and Freundlich isotherm models. The data showed that the adsorption behavior of the AO-wood was more related to Langmuir models (monolayer adsorption). The excellent uranium uptake performance ( $1375 \text{ mg g}^{-1}$ ) was comparable or superior to other reported biopolymer and synthetic polymer-based adsorbents.

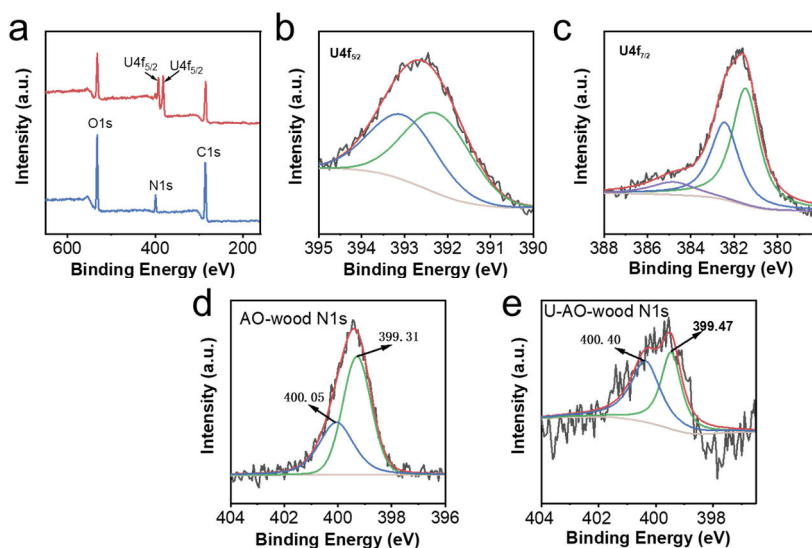


**Figure 4.28.** a) XPS spectra of the AO-wood for uranium adsorption. b and c) High-resolution XPS spectra of the two U4f peaks of the U-uptake AO-wood. High-resolution XPS spectrum of nitrogen element in AO-wood (d) before and (e) after adsorption, respectively.

To further analyze the detailed chemisorption process, the uranium uploaded AO-wood was investigated by XPS. In comparison to the XPS spectrum of AO-wood, the new strong U4f peaks appeared after uranium uptake (**Figure 4.28a**). Meanwhile, the U 4f<sub>5/2</sub> (392.50 eV) and U 4f<sub>7/2</sub> (381.70 eV) were also observed from the high-resolution spectrum of U (**Figure 4.28b** and **Figure 4.28c**), respectively, further supporting the adsorption of uranyl ions on the AO-wood. Moreover, the peaks at 399.31 and 400.05 eV in the high-resolution spectrum of N were attributed to C-NH<sub>2</sub> and C=NOH (**Figure 4.28d** and **Figure 4.28e**), respectively.[177, 178] After U adsorption, the changes of intensity and binding energy indicated the strong interaction between nitrogen-containing functional groups and uranyl ions.[175, 178]

#### 4.5.4 Regeneration and reusability

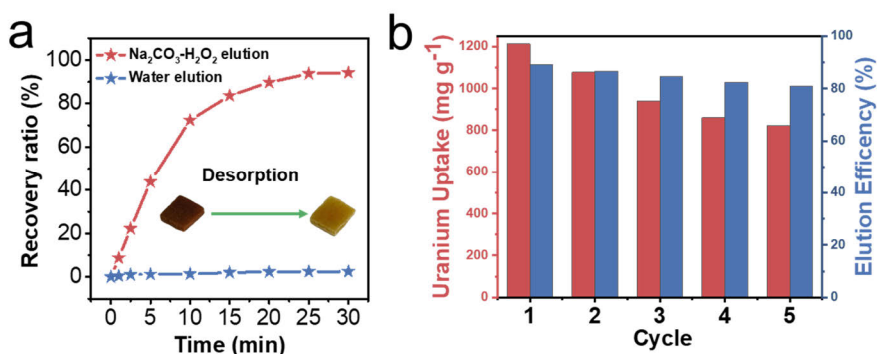


**Figure 4.29.** a) Desorption kinetics in the elution solution. b) Cyclic adsorption-recovery performance of the reversible absorption.

The regeneration performance of the AO-wood was investigated by regenerating the samples in the elute (1 M  $\text{Na}_2\text{CO}_3$  and 0.1 M  $\text{H}_2\text{O}_2$ ). **Figure 4.29a** shows that over 94% of captured uranium was desorbed rapidly within 30 min via the formation of extremely stable uranyl-peroxo-carbonato complex.[179] In addition, an efficient regeneration process was also demonstrated by the change in the color of the sample from red to light yellow. Then 5 adsorption-desorption processes were carried out to evaluate the reusability (**Figure 4.29b**). The uptake performance was maintained with 821  $\text{mg g}^{-1}$ , and the elution efficiency reached over 80%, indicating an excellent regenerability and recyclability of AO-wood. The slight deterioration of the adsorption-desorption processes was mainly due to the residual uranyl ions occupying the adsorption sites.

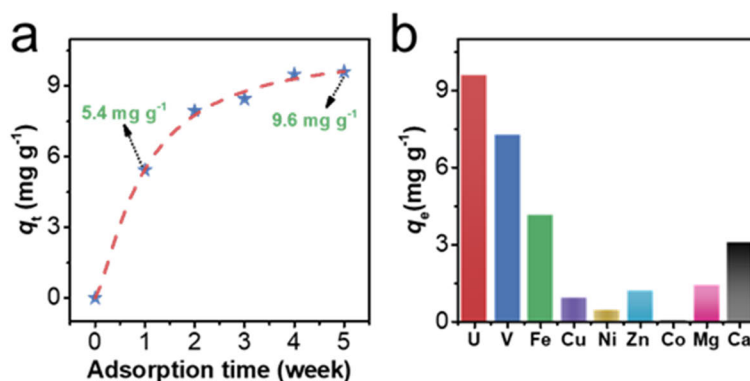


**Figure 4.30.** a) Kinetics of AO-wood for uranium uptake in real seawater. b) Selectivity uptake capacities of AO-wood to other co-existing ions.

The uranium uptake performance of AO-wood in natural seawater was also investigated. Briefly, 4 mg AO-wood were immersed in 50 L natural seawater for 7, 14, 21, 30, and 35 days, respectively. Then samples were collected and digested under microwave digestion for 1 h and the loaded uranium amount was

calculated by ICP-MS. The results showed a high uranium adsorption capacity with  $5.70 \text{ mg g}^{-1}$  was achieved in the first 7 days, and the maximum uranium uptake can reach  $9.6 \text{ mg g}^{-1}$  after soaking for 35 days (**Figure 4.30a**). In addition, the AO-wood also exhibited excellent selective extraction for uranium ions compared to other metal ions in natural seawater (**Figure 4.30b**).

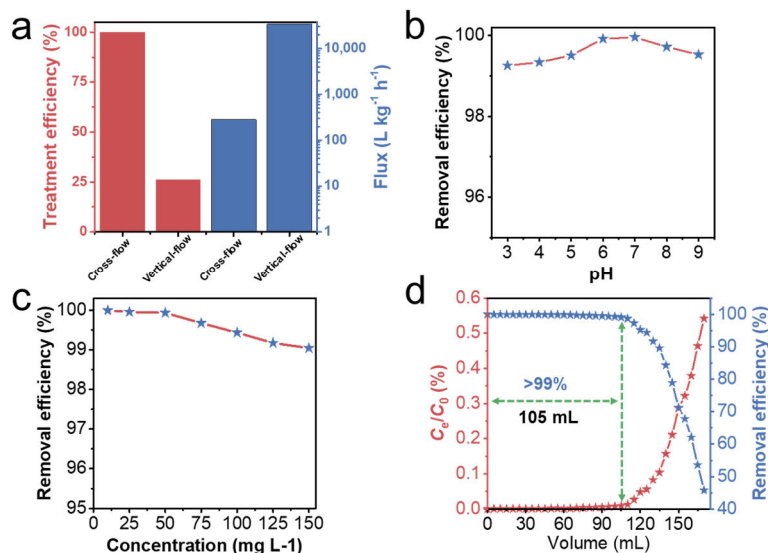


**Figure 4.31.** a) Comparison of treatment efficiency and treatment speed between the cross-flow and vertical-flow. The effect of (b) pH and (c) uranium concentration on the uranium treatment efficiency. d) The breakthrough profiles and removal efficiency of the AO-wood membrane for uranium adsorption with an initial uranium concentration at  $50 \text{ mg L}^{-1}$  at pH 8.

We further investigated the highly efficient uranium ion removal by the obtained mesoporous AO-wood membrane. When the uranium ions passed through the AO-wood membrane, they could be captured by the abundant amidoxime groups on the surface of pore walls. To better take advantage of the wood structure for uranium ion filtration, we compared its removal performance and water transportation in cross-flow and vertical-flow with a 2 mm thick wood membrane (**Figure 4.31a**). A fast flow rate was achieved ( $3.4 \times 10^4 \text{ L kg}^{-1} \text{ h}^{-1}$ ) for the vertical-flow with a relatively low removal efficiency (26.2%), mainly due to the megalopores. In addition, a treatment speed of  $\sim 280 \text{ L kg}^{-1} \text{ h}^{-1}$  was achieved for the cross-flow filtration device and the efficiency reached  $\sim 99.9\%$ . Therefore, the cross-flow can better utilize the pits and nanopores connecting the wood vessel channels to reach an excellent treatment efficiency. We further analyzed the uranium filtration efficiency in the pH range of 3–9 in **Figure 4.31b**. The wood membrane exhibited excellent filtration efficiency ( $\sim 99.26\%$ ) at all pH values, which is vital for the device to be used in different conditions. Furthermore, this membrane presented excellent uranium treatment efficiency ( $\sim 99\%$ ) even at a high initial uranium concentration ( $150 \text{ mg L}^{-1}$ ) (**Figure 4.31c**). The breakthrough behaviors of the wood membrane were further studied,

as shown in **Figure 4.31d**. Remarkably, a high uranium removal ratio ( $> 99\%$ ) could be maintained in the filtration of 105 mL uranium-containing wastewater ( $50 \text{ mg L}^{-1}$ ), with adsorption capacity was high to  $\sim 288.5 \text{ mg g}^{-1}$ .

## 5. Conclusions and future perspectives

### 5.1 Highlights of the thesis

This work aimed to the comprehensive development of wood-derived nanostructured materials for wastewater treatment. Different types of nanocellulose were prepared based on a deep understanding of the physical and chemical properties of cellulose.

We firstly produced CNFs by TEMPO-mediated oxidation. Then the CNF-based composite aerogel was fabricated by combining with PEI and then decorated with Ag NPs. The obtained composite aerogel showed a microporous structure, rapid water-activated shape memory, and excellent structure stability in test conditions. In addition, the aerogels exhibited excellent catalytic discoloration properties towards anionic and cationic dyes. More importantly, the catalytic activity kept stable after a long-time test, and the discoloration efficiency remained over 98% after 10 times cycles with a rapid transportation  $5 \times 10^4 \text{ L} \cdot \text{m}^{-2} \text{ h}^{-1}$ .

Furthermore, physical and chemical cross-linking were applied to design and fabricate CNF/PEI composite aerogels via physical and chemical cross-linking with epichlorohydrin (ECH). The dual cross-linked aerogel exhibited high water resistance in different water environments, fast water-activated shape memory, and rapid water transportation. The CNF/PEI exhibited excellent static uptake capacity ( $1226 \text{ mg g}^{-1}$ ) and dynamic uptake capacity ( $960 \text{ mg g}^{-1}$ ) for the MO. Remarkably, the CNF/PEI aerogel presented outstanding selection removal ability for separating cationic and anionic dye mixtures.

Moreover, we prepared AO-CNF through an energy-efficiency, high-yield, and two-step procedure. The resultant AO-CNF exhibited rapid kinetics ( $<5 \text{ min}$ ) and high adsorption capacity ( $1327 \text{ mg g}^{-1}$ ). The AO-CNF can also make them to fabricate fibrous porous membranes, which can be used for uranium capturing in continuous flow filtration. In the case of a  $2.5 \mu\text{m}$  thick membrane, it could afford an ultra-high water transport ( $\sim 48 \text{ L m}^{-2} \text{ h}^{-1}$ ) and excellent treatment efficiency (99.9%).

Lastly, AO-wood aerogel with a highly mesoporous structure was directly fabricated from native balsa wood through cyanoethylation and amidoximation. The obtained AO-wood exhibited excellent mechanical performance and high specific surface area. The adsorption capacity towards uranium was high in the pH range of 3–9, and the highest uptake ability reached  $1375 \text{ mg g}^{-1}$ . In real seawater, the AO-wood presents a high uranium extraction capacity of  $9.6 \text{ mg g}^{-1}$  after soaking for 5 weeks. More importantly, the AO-wood's unique structure can make it a filter to remove uranium ions by efficient filtration.

### 5.2 Future perspectives

Wood-derived biopolymers as the most important renewable materials are promising candidates to replace synthetic polymers in the field of wastewater

treatment. Nanocellulose has been developed to fabricate supports, membranes, and aerogels. However, these nanocellulose-based materials were generally produced by a “bottom-up” approach, which undergoes a series of processes (physical and chemical treatment, and reassembling). This complicated approach is time-and-energy-consuming, which obstructs the large-scale production and applications of biopolymer nanofibrils materials. Therefore, fabricating functional nanocellulose-based materials efficiently with low cost is still a big challenge in the future.

## 6. Acknowledgments

This doctoral thesis work was accomplished in the Laboratory of Natural Materials Technology at the Faculty of Science and Engineering at Åbo Akademi University during the time of 11.2017-01.2022. Many thanks for the financial support from the China Scholarship Council, Harry Elvings Legat, and Rector's funds and mobility funds from Åbo Akademi University, as well as the funding from CAS Key Laboratory of Bio-based Materials during my research visit to Qingdao Institute of Bioenergy and Bioprocess Technology, Chinese Academy of Sciences.

I would like to express my sincerest gratitude to Professor Stefan Willför and Professor Chunlin Xu for their supervision and endless help. Many thanks to Professor Stefan Willför to provide this opportunity and platform for my doctoral research study. I still remember the encouragement that he said to me: scientific research work is not always easy. Professor Chunlin Xu always stands behind me whenever I need help. It seems like he is always convenient when I want to have a discussion. Every time, he can give some non-absolute answers to me, which significantly guided me to the right answers. His patience with students and attitude to work made him a model to me. He also provided many opportunities for applying for funding and offered me a chance to visit abroad to enrich my research experience. Thanks!!! 感谢!!! I would also like to thank Dr. Xiaojun Wang (a co-supervisor) for her help and patience during my research work. She encouraged me a lot to try new areas and give me lots of support. For example, when she knew that I need a Xe light, she immediately drove me to several supermarkets to "search" the light. These memories are valuable and still hang on my head. A big thank to Docent Anna Sundberg, who offered me many opportunities to practice my English language and gave me so much help and valuable suggestions in my research work.

My gratitude goes to Professor Chaoxu Li for offering me the opportunity to visit the Group of Biomimetic Smart Materials, CAS Key Laboratory of Bio-based Materials, Qingdao Institute of Bioenergy and Bioprocess Technology, Chinese Academy of Sciences. The time in CAS broadened my sights and views and was helpful to my research career. Many thanks also to Professor Mingjie Li for the numerous help and guidance during my research work. He showed me a lot of skills about many softwares and how to think to improve my work. These experiences are valuable for me to continue my research work in the future. I would also like to express my gratitude to Professor Jun You, who is always online to answer my questions.

I also thank all the present and former colleagues working in the same lab. Especially Andrey Pranovich, Jarl Hemming, Annika Smeds, Wenyang Xu, Yongchao Zhang, Liqiu Hu, Luyao Wang, Qingbo Wang, Rui Liu, Huanfei Xu, Ekaterina Korotkova, Yury Brusentsev, Bin Li, Xiankai Li, Lili Lv, Xinpeng Che, Xiao Han, and Lifan Long. Thanks for their assistance, good memories in

the lab together, and joys. I also would like to thank all the co-authors for providing valuable help in the research work.

Many thanks to all my friends in Turku. Thanks for the “good times” together!!! These valuable memories will be remembered forever.

Finally, I would like to express my gratitude to my girlfriend and loving families for their endless love and support. I love you all!!!

## 7. References

1. Jamil, M., Zia, M. S., Qasim, M., 2010. Contamination of agro-ecosystem and human health hazards from wastewater used for irrigation. *Journal of the Chemical Society of Pakistan*, **32**, 370-378.
2. Khan, S., Cao, Q., Zheng, Y., Huang, Y., Zhu, Y., 2008. Health risks of heavy metals in contaminated soils and food crops irrigated with wastewater in Beijing, China. *Environmental Pollution*, **152**, 686-692.
3. Tiwari, J. N., Mahesh, K., Le, N. H., Kemp, K. C., Timilsina, R., Tiwari, R. N., Kim, K. S., 2013. Reduced graphene oxide-based hydrogels for the efficient capture of dye pollutants from aqueous solutions. *Carbon*, **56**, 173-182.
4. Raghu, S., Basha, C. A., 2007. Chemical or electrochemical techniques, followed by ion exchange, for recycle of textile dye wastewater. *Journal of Hazardous materials*, **149**, 324-330.
5. Li, S., Wang, W., Liu, Y., Zhang, W.-x., 2014. Zero-valent iron nanoparticles (nZVI) for the treatment of smelting wastewater: a pilot-scale demonstration. *Chemical Engineering Journal*, **254**, 115-123.
6. Oliveira, L. C., Coura, C. V. Z., Guimarães, I. R., Gonçalves, M., 2011. Removal of organic dyes using Cr-containing activated carbon prepared from leather waste. *Journal of Hazardous materials*, **192**, 1094-1099.
7. Yang, M., Zhang, Y., Shao, B., Qi, R., Myoga, H., 2001. Precipitative removal of fluoride from electronics wastewater. *Journal of Environmental Engineering*, **127**, 902-907.
8. Hu, X.-F., Jiang, Y., Shu, Y., Hu, X., Liu, L., Luo, F., 2014. Effects of mining wastewater discharges on heavy metal pollution and soil enzyme activity of the paddy fields. *Journal of Geochemical Exploration*, **147**, 139-150.
9. Hailei, W., Guangli, Y., Guosheng, L., Feng, P., 2006. A new way to cultivate aerobic granules in the process of papermaking wastewater treatment. *Biochemical Engineering Journal*, **28**, 99-103.
10. Khan, Z. I., Ugulu, I., Ahmad, K., Yasmeen, S., Noorka, I. R., Mehmood, N., Sher, M., 2018. Assessment of trace metal and metalloid accumulation and human health risk from vegetables consumption through spinach and coriander specimens irrigated with wastewater. *Bulletin of environmental contamination and toxicology*, **101**, 787-795.
11. Manatunga, D., De Silva, R., De Silva, K., De Silva, N., Premalal, E. (2018).
12. Mittal, A., Malviya, A., Kaur, D., Mittal, J., Kurup, L., 2007. Studies on the adsorption kinetics and isotherms for the removal and recovery of Methyl Orange from wastewaters using waste materials. *Journal of Hazardous materials*, **148**, 229-240.
13. Stafiej, A., Pyrzynska, K., 2007. Adsorption of heavy metal ions with carbon nanotubes. *Separation and Purification Technology*, **58**, 49-52.
14. Dąbrowski, A., Hubicki, Z., Podkościelny, P., Robens, E., 2004. Selective removal of the heavy metal ions from waters and industrial wastewaters by ion-exchange method. *Chemosphere*, **56**, 91-106.
15. Ngah, W. W., Teong, L., Hanafiah, M. M., 2011. Adsorption of dyes and heavy metal ions by chitosan composites: A review. *Carbohydrate Polymers*, **83**, 1446-1456.
16. Devi, P., Kumar, P., 2020. Concept and application of phytoremediation in the fight of heavy metal toxicity. *Journal of Pharmaceutical Sciences and Research*, **12**, 795-804.
17. Awual, M. R., Hasan, M. M., 2015. Colorimetric detection and removal of copper (II) ions from wastewater samples using tailor-made composite adsorbent. *Sensors and Actuators B: Chemical*, **206**, 692-700.
18. Zhang, W., Wang, X., Zhang, Y., van Bochove, B., Mäkilä, E., Seppälä, J., Xu, W., Willför, S., Xu, C., 2020. Robust shape-retaining nanocellulose-based aerogels decorated with

- silver nanoparticles for fast continuous catalytic discoloration of organic dyes. *Separation and Purification Technology*, **242**, 116523.
19. Gao, Y., Deng, S.-Q., Jin, X., Cai, S.-L., Zheng, S.-R., Zhang, W.-G., 2019. The construction of amorphous metal-organic cage-based solid for rapid dye adsorption and time-dependent dye separation from water. *Chemical Engineering Journal*, **357**, 129-139.
  20. Tong, M., Liu, D., Yang, Q., Devautour-Vinot, S., Maurin, G., Zhong, C., 2013. Influence of framework metal ions on the dye capture behavior of MIL-100 (Fe, Cr) MOF type solids. *Journal of Materials Chemistry A*, **1**, 8534-8537.
  21. DeCoste, J. B., Peterson, G. W., 2014. Metal-organic frameworks for air purification of toxic chemicals. *Chemical Reviews*, **114**, 5695-5727.
  22. Ramalingam, B., Khan, M. M. R., Mondal, B., Mandal, A. B., Das, S. K., 2015. Facile synthesis of silver nanoparticles decorated magnetic-chitosan microsphere for efficient removal of dyes and microbial contaminants. *ACS Sustainable Chemistry & Engineering*, **3**, 2291-2302.
  23. Liu, N., Zhang, W., Li, X., Qu, R., Zhang, Q., Wei, Y., Feng, L., Jiang, L., 2017. Fabrication of robust mesh with anchored Ag nanoparticles for oil removal and in situ catalytic reduction of aromatic dyes. *Journal of Materials Chemistry A*, **5**, 15822-15827.
  24. Chu, Z., Feng, Y., Seeger, S., 2015. Oil/Water Separation with Selective Superantwetting/Superwetting Surface Materials. *Angewandte Chemie International Edition*, **54**, 2328-2338.
  25. Gupta, R. K., Dunderdale, G. J., England, M. W., Hozumi, A., 2017. Oil/water separation techniques: a review of recent progresses and future directions. *Journal of Materials Chemistry A*, **5**, 16025-16058.
  26. Hayase, G., Kanamori, K., Fukuchi, M., Kaji, H., Nakanishi, K., 2013. Facile synthesis of marshmallow-like macroporous gels usable under harsh conditions for the separation of oil and water. *Angewandte Chemie*, **125**, 2040-2043.
  27. Xu, S., Hasselblad, S., 1996. A simple biological method to estimate the readily biodegradable organic matter in wastewater. *Water Research*, **30**, 1023-1025.
  28. Ksibi, M., 2006. Chemical oxidation with hydrogen peroxide for domestic wastewater treatment. *Chemical Engineering Journal*, **119**, 161-165.
  29. Li, X., Liu, H., Cheng, L., Tong, H., 2003. Photocatalytic oxidation using a new catalyst TiO<sub>2</sub> microsphere for water and wastewater treatment. *Environmental science & technology*, **37**, 3989-3994.
  30. Obotey Ezugbe, E., Rathilal, S., 2020. Membrane technologies in wastewater treatment: a review. *Membranes*, **10**, 89.
  31. De Gisi, S., Lofrano, G., Grassi, M., Notarnicola, M., 2016. Characteristics and adsorption capacities of low-cost sorbents for wastewater treatment: A review. *Sustainable Materials and Technologies*, **9**, 10-40.
  32. Adusei-Gyamfi, J., Ouddane, B., Rietveld, L., Cornard, J.-P., Criquet, J., 2019. Natural organic matter-cations complexation and its impact on water treatment: A critical review. *Water Research*, **160**, 130-147.
  33. Greenlee, L. F., Lawler, D. F., Freeman, B. D., Marrot, B., Moulin, P., 2009. Reverse osmosis desalination: water sources, technology, and today's challenges. *Water Research*, **43**, 2317-2348.
  34. Maleki, H., Hüsing, N., 2018. Current status, opportunities and challenges in catalytic and photocatalytic applications of aerogels: Environmental protection aspects. *Applied Catalysis B: Environmental*, **221**, 530-555.
  35. Kistler, S. S., 1931. Coherent expanded aerogels and jellies. *Nature*, **127**, 741-741.
  36. Wu, D., Sun, Z., Fu, R., 2006. Structure and adsorption properties of activated carbon aerogels. *Journal of Applied Polymer Science*, **99**, 2263-2267.

37. Wang, H., Gong, Y., Wang, Y., 2014. Cellulose-based hydrophobic carbon aerogels as versatile and superior adsorbents for sewage treatment. *Rsc Advances*, **4**, 45753-45759.
38. Anderson, A. M., Carroll, M. K., 2011. Hydrophobic silica aerogels: review of synthesis, properties and applications. *Aerogels handbook*, 47-77.
39. Rao, A. P., Rao, A. V., 2008. Microstructural and physical properties of the ambient pressure dried hydrophobic silica aerogels with various solvent mixtures. *Journal of Non-Crystalline Solids*, **354**, 10-18.
40. Barrios, E., Fox, D., Li Sip, Y. Y., Catarata, R., Calderon, J. E., Azim, N., Afrin, S., Zhang, Z., Zhai, L., 2019. Nanomaterials in advanced, high-performance aerogel composites: a review. *Polymers*, **11**, 726.
41. Lamy-Mendes, A., Silva, R. F., Durães, L., 2018. Advances in carbon nanostructure–silica aerogel composites: a review. *Journal of Materials Chemistry A*, **6**, 1340-1369.
42. Ulker, Z., Erkey, C., 2014. An emerging platform for drug delivery: Aerogel based systems. *Journal of Controlled Release*, **177**, 51-63.
43. Du, A., Zhou, B., Zhang, Z., Shen, J., 2013. A special material or a new state of matter: a review and reconsideration of the aerogel. *Materials*, **6**, 941-968.
44. Wei, S., Ching, Y. C., Chuah, C. H., 2020. Synthesis of chitosan aerogels as promising carriers for drug delivery: A review. *Carbohydrate Polymers*, **231**, 115744.
45. Wang, L., Xu, H., Gao, J., Yao, J., Zhang, Q., 2019. Recent progress in metal-organic frameworks-based hydrogels and aerogels and their applications. *Coordination Chemistry Reviews*, **398**, 213016.
46. Jiang, F., Dinh, D. M., Hsieh, Y.-L., 2017. Adsorption and desorption of cationic malachite green dye on cellulose nanofibril aerogels. *Carbohydrate Polymers*, **173**, 286-294.
47. Liu, H., Geng, B., Chen, Y., Wang, H., 2017. Review on the aerogel-type oil sorbents derived from nanocellulose. *ACS sustainable chemistry & engineering*, **5**, 49-66.
48. Meena, A. K., Mishra, G., Rai, P., Rajagopal, C., Nagar, P., 2005. Removal of heavy metal ions from aqueous solutions using carbon aerogel as an adsorbent. *Journal of Hazardous materials*, **122**, 161-170.
49. Jin, Y., Wu, M., Zhao, G., Li, M., 2011. Photocatalysis-enhanced electrosorption process for degradation of high-concentration dye wastewater on TiO<sub>2</sub>/carbon aerogel. *Chemical Engineering Journal*, **168**, 1248-1255.
50. Yang, M. Q., Tan, C. F., Lu, W., Zeng, K., Ho, G. W., 2020. Spectrum Tailored Defective 2D Semiconductor Nanosheets Aerogel for Full - Spectrum - Driven Photothermal Water Evaporation and Photochemical Degradation. *Advanced Functional Materials*, **30**, 2004460.
51. Ganesamoorthy, R., Vadivel, V. K., Kumar, R., Kushwaha, O. S., Mamane, H., 2021. Aerogels for water treatment: a review. *Journal of Cleaner Production*, **329**, 129713.
52. Payen, A., 1838. Mémoire sur la composition du tissu propre des plantes et du ligneux. *Comptes rendus*, **7**, 1052-1056.
53. Wang, S., Lu, A., Zhang, L., 2016. Recent advances in regenerated cellulose materials. *Progress in Polymer Science*, **53**, 169-206.
54. Updegraff, D. M., 1969. Semimicro determination of cellulose in biological materials. *Analytical Biochemistry*, **32**, 420-424.
55. Hinterstoesser, B., Salmén, L., 2000. Application of dynamic 2D FTIR to cellulose. *Vibrational Spectroscopy*, **22**, 111-118.
56. Li, Q., Renneckar, S., 2011. Supramolecular structure characterization of molecularly thin cellulose I nanoparticles. *Biomacromolecules*, **12**, 650-659.
57. Neralla, S., *Nanocrystals: Synthesis, Characterization and Applications*. (BoD–Books on Demand, 2012).

58. Klemm, D., Cranston, E. D., Fischer, D., Gama, M., Kedzior, S. A., Kralisch, D., Kramer, F., Kondo, T., Lindström, T., Nietzsche, S., 2018. Nanocellulose as a natural source for groundbreaking applications in materials science: Today's state. *Materials Today*, **21**, 720-748.
59. Shi, Z., Zhang, Y., Phillips, G. O., Yang, G., 2014. Utilization of bacterial cellulose in food. *Food hydrocolloids*, **35**, 539-545.
60. de Oliveira Barud, H. G., da Silva, R. R., da Silva Barud, H., Tercjak, A., Gutierrez, J., Lustri, W. R., de Oliveira Junior, O. B., Ribeiro, S. J., 2016. A multipurpose natural and renewable polymer in medical applications: Bacterial cellulose. *Carbohydrate Polymers*, **153**, 406-420.
61. Hu, Y., Liu, F., Sun, Y., Xu, X., Chen, X., Pan, B., Sun, D., Qian, J., 2019. Bacterial cellulose derived paper-like purifier with multifunctionality for water decontamination. *Chemical Engineering Journal*, **371**, 730-737.
62. Iguchi, M., Yamanaka, S., Budhiono, A., 2000. Bacterial cellulose—a masterpiece of nature's arts. *Journal of materials science*, **35**, 261-270.
63. Nogi, M., Yano, H., 2008. Transparent nanocomposites based on cellulose produced by bacteria offer potential innovation in the electronics device industry. *Advanced Materials*, **20**, 1849-1852.
64. Klemm, D., Kramer, F., Moritz, S., Lindström, T., Ankerfors, M., Gray, D., Dorris, A., 2011. Nanocelluloses: a new family of nature-based materials. *Angewandte Chemie International Edition*, **50**, 5438-5466.
65. Lizundia, E., Costa, C. M., Alves, R., Lanceros-Méndez, S., 2020. Cellulose and its derivatives for lithium ion battery separators: A review on the processing methods and properties. *Carbohydrate Polymer Technologies and Applications*, **1**, 100001.
66. Calvino, C., Macke, N., Kato, R., Rowan, S. J., 2020. Development, processing and applications of bio-sourced cellulose nanocrystal composites. *Progress in Polymer Science*, **103**, 101221.
67. Nechyporchuk, O., Belgacem, M. N., Bras, J., 2016. Production of cellulose nanofibrils: A review of recent advances. *Industrial Crops and Products*, **93**, 2-25.
68. Wang, J., Tavakoli, J., Tang, Y., 2019. Bacterial cellulose production, properties and applications with different culture methods—A review. *Carbohydrate Polymers*, **219**, 63-76.
69. Ribeiro, R. S., Pohlmann, B. C., Calado, V., Bojorge, N., Pereira Jr, N., 2019. Production of nanocellulose by enzymatic hydrolysis: Trends and challenges. *Engineering in Life Sciences*, **19**, 279-291.
70. Nickerson, R., Habrle, J., 1947. Cellulose intercrystalline structure. *Industrial & Engineering Chemistry*, **39**, 1507-1512.
71. Beck-Candanedo, S., Roman, M., Gray, D. G., 2005. Effect of reaction conditions on the properties and behavior of wood cellulose nanocrystal suspensions. *Biomacromolecules*, **6**, 1048-1054.
72. Habibi, Y., Lucia, L. A., Rojas, O. J., 2010. Cellulose nanocrystals: chemistry, self-assembly, and applications. *Chemical Reviews*, **110**, 3479-3500.
73. Elazzouzi-Hafraoui, S., Nishiyama, Y., Putaux, J., Heux, L., Dubreuil, F., Rochas, C., 2008. The Shape and Size Distribution of Crystalline Nanoparticles PrepThe shape and size distribution of crystalline nanoparticles prepared by acid hydrolysis of native cellulose. *Biomacromolecules*, **9**, 57-65.
74. Nagarajan, K., Balaji, A., Rajan, S. T. K., Basha, K. S., 2019. Effect of sulfuric acid reaction time on the properties and behavior of cellulose nanocrystals from *Cocos nucifera* var-Aurantiaca peduncle's cellulose microfibrils. *Materials Research Express*, **6**, 125333.

75. Nagarajan, K., Ramanujam, N., Sanjay, M., Siengchin, S., Surya Rajan, B., Sathick Basha, K., Madhu, P., Raghav, G., 2021. A comprehensive review on cellulose nanocrystals and cellulose nanofibers: Pretreatment, preparation, and characterization. *Polymer Composites*, **42**, 1588-1630.
76. Shang, Z., An, X., Seta, F. T., Ma, M., Shen, M., Dai, L., Liu, H., Ni, Y., 2019. Improving dispersion stability of hydrochloric acid hydrolyzed cellulose nano-crystals. *Carbohydrate Polymers*, **222**, 115037.
77. Cheng, M., Qin, Z., Chen, Y., Liu, J., Ren, Z., 2017. Facile one-step extraction and oxidative carboxylation of cellulose nanocrystals through hydrothermal reaction by using mixed inorganic acids. *Cellulose*, **24**, 3243-3254.
78. Jinzhao, L., Zheng, L., Xupin, Z., Jixian, G., Qiujin, L., Jianfei, Z., 2021. Preparation of Cellulose Nanocrystallines and Their Applications in Composite Materials. *Progress in Chemistry*, **33**, 1293.
79. Davis, N. J., Flitsch, S. L., 1993. Selective oxidation of monosaccharide derivatives to uronic acids. *Tetrahedron Letters*, **34**, 1181-1184.
80. Saito, T., Isogai, A., 2006. Introduction of aldehyde groups on surfaces of native cellulose fibers by TEMPO-mediated oxidation. *Colloids and Surfaces A: Physicochemical and Engineering Aspects*, **289**, 219-225.
81. Isogai, A., Saito, T., Fukuzumi, H., 2011. TEMPO-oxidized cellulose nanofibers. *nanoscale*, **3**, 71-85.
82. Isogai, A., Saito, T., Fukuzumi, H. (2011).
83. Mishra, S. P., Manent, A.-S., Chabot, B., Daneault, C., 2012. The use of sodium chlorite in post-oxidation of TEMPO-oxidized pulp: Effect on pulp characteristics and nanocellulose yield. *Journal of Wood Chemistry and Technology*, **32**, 137-148.
84. Herrick, F. W., Casebier, R. L., Hamilton, J. K., Sandberg, K. R., in *J. Appl. Polym. Sci.: Appl. Polym. Symp. (United States)*. (ITT Rayonier Inc., Shelton, WA, 1983), vol. 37.
85. Zimmermann, T., Pöhler, E., Geiger, T., 2004. Cellulose fibrils for polymer reinforcement. *Advanced Engineering Materials*, **6**, 754-761.
86. Ankerfors, M., Aulin, C., Lindström, T., in *2011 TAPPI International conference on nanotechnology for renewable materials, Washington DC, USA, 6-8 June 2011*. (2011).
87. Nakagaito, A., Iwamoto, S., Yano, H., 2005. Bacterial cellulose: the ultimate nanoscalar cellulose morphology for the production of high-strength composites. *Applied Physics A*, **80**, 93-97.
88. Brown, A. J., 1886. XLIII.—On an acetic ferment which forms cellulose. *Journal of the Chemical Society, Transactions*, **49**, 432-439.
89. Jonas, R., Farah, L. F., 1998. Production and application of microbial cellulose. *Polymer Degradation and Stability*, **59**, 101-106.
90. Abraham, A., Jothi, V. R., Lee, J., Yi, S.-C., Sang, B.-I., 2020. Bacterial nanocellulose as a green and flexible electrode matrix for efficient hydrogen evolution reaction in alkaline conditions. *Cellulose*, **27**, 8135-8146.
91. Li, K., Wang, S., Chen, H., Yang, X., Berglund, L. A., Zhou, Q., 2020. Self-Densification of Highly Mesoporous Wood Structure into a Strong and Transparent Film. *Advanced Materials*, **32**, 2003653.
92. Garemark, J., Yang, X., Sheng, X., Cheung, O., Sun, L., Berglund, L. A., Li, Y., 2020. Top-down approach making anisotropic cellulose aerogels as universal substrates for multifunctionalization. *ACS nano*, **14**, 7111-7120.
93. Guan, H., Cheng, Z., Wang, X., 2018. Highly Compressible Wood Sponges with a Spring-like Lamellar Structure as Effective and Reusable Oil Absorbents. *ACS Nano*, **12**, 10365-10373.

94. Song, J., Chen, C., Yang, Z., Kuang, Y., Li, T., Li, Y., Huang, H., Kierzewski, I., Liu, B., He, S., 2018. Highly compressible, anisotropic aerogel with aligned cellulose nanofibers. *ACS nano*, **12**, 140-147.
95. Chen, Y., Zhang, L., Yang, Y., Pang, B., Xu, W., Duan, G., Jiang, S., Zhang, K., 2021. Recent Progress on Nanocellulose Aerogels: Preparation, Modification, Composite Fabrication, Applications. *Advanced Materials*, **33**, 2005569.
96. Shahnaz, T., Sharma, V., Subbiah, S., Narayanasamy, S., 2020. Multivariate optimisation of Cr (VI), Co (III) and Cu (II) adsorption onto nanobentonite incorporated nanocellulose/chitosan aerogel using response surface methodology. *Journal of Water Process Engineering*, **36**, 101283.
97. Abou-Zeid, R. E., Ali, K. A., Gawad, R. M., Kamal, K. H., Kamel, S., Khiari, R., 2021. Removal of Cu (II), Pb (II), Mg (II), and Fe (II) by Adsorption onto Alginate/Nanocellulose Beads as Bio-Sorbent. *Journal of Renewable Materials*, **9**, 601.
98. Mo, L., Pang, H., Tan, Y., Zhang, S., Li, J., 2019. 3D multi-wall perforated nanocellulose-based polyethylenimine aerogels for ultrahigh efficient and reversible removal of Cu (II) ions from water. *Chemical Engineering Journal*, **378**, 122157.
99. Zheng, Q., Cai, Z., Gong, S., 2014. Green synthesis of polyvinyl alcohol (PVA)–cellulose nanofibril (CNF) hybrid aerogels and their use as superabsorbents. *Journal of materials chemistry A*, **2**, 3110-3118.
100. Zarei, S., Niad, M., Raanaei, H., 2018. The removal of mercury ion pollution by using Fe<sub>3</sub>O<sub>4</sub>-nanocellulose: Synthesis, characterizations and DFT studies. *Journal of Hazardous materials*, **344**, 258-273.
101. Yu, H., Zhang, S., Wang, Y., Yin, D., Huang, J., 2021. Covalent modification of Nanocellulose (NCC) by functionalized Graphene oxide (GO) and the study of adsorption mechanism. *Composite Interfaces*, **28**, 145-158.
102. Shaheed, N., Javanshir, S., Esmkhani, M., Dekamin, M. G., Naimi-Jamal, M. R., 2021. Synthesis of nanocellulose aerogels and Cu-BTC/nanocellulose aerogel composites for adsorption of organic dyes and heavy metal ions. *Scientific Reports*, **11**, 1-11.
103. Núñez, D., Cáceres, R., Ide, W., Varaprasad, K., Oyarzún, P., 2020. An ecofriendly nanocomposite of bacterial cellulose and hydroxyapatite efficiently removes lead from water. *International Journal of Biological Macromolecules*, **165**, 2711-2720.
104. Li, J., Zuo, K., Wu, W., Xu, Z., Yi, Y., Jing, Y., Dai, H., Fang, G., 2018. Shape memory aerogels from nanocellulose and polyethyleneimine as a novel adsorbent for removal of Cu (II) and Pb (II). *Carbohydrate Polymers*, **196**, 376-384.
105. Geng, B., Wang, H., Wu, S., Ru, J., Tong, C., Chen, Y., Liu, H., Wu, S., Liu, X., 2017. Surface-Tailored Nanocellulose Aerogels with Thiol-Functional Moieties for Highly Efficient and Selective Removal of Hg(II) Ions from Water. *ACS Sustainable Chemistry & Engineering*, **5**, 11715-11726.
106. Wei, J., Yang, Z., Sun, Y., Wang, C., Fan, J., Kang, G., Zhang, R., Dong, X., Li, Y., 2019. Nanocellulose-based magnetic hybrid aerogel for adsorption of heavy metal ions from water. *Journal of Materials Science*, **54**, 6709-6718.
107. Zhu, L., Zong, L., Wu, X., Li, M., Wang, H., You, J., Li, C., 2018. Shapeable Fibrous Aerogels of Metal–Organic-Frameworks Templated with Nanocellulose for Rapid and Large-Capacity Adsorption. *ACS Nano*, **12**, 4462-4468.
108. Alle, M., Bandi, R., Sharma, G., Lee, S.-H., Kim, J.-C., 2021. Shape recoverable, Au nanoparticles loaded nanocellulose foams as a recyclable catalyst for the dynamic and batch discoloration of dyes. *Carbohydrate Polymers*, **258**, 117693.
109. Ferreira-Neto, E. P., Ullah, S., da Silva, T. C., Domenegueti, R. R., Perissinotto, A. P., de Vicente, F. S., Rodrigues-Filho, U. P., Ribeiro, S. J., 2020. Bacterial nanocellulose/MoS<sub>2</sub> hybrid aerogels as bifunctional adsorbent/photocatalyst

- membranes for in-flow water decontamination. *ACS Applied Materials & Interfaces*, **12**, 41627-41643.
110. Ma, Z., Zhou, P., Zhang, L., Zhong, Y., Sui, X., Wang, B., Ma, Y., Feng, X., Xu, H., Mao, Z., 2021. A recyclable 3D g-C<sub>3</sub>N<sub>4</sub> based nanocellulose aerogel composite for photodegradation of organic pollutants. *Cellulose*, **28**, 3531-3547.
  111. Mohammed, N., Grishkewich, N., Berry, R. M., Tam, K. C., 2015. Cellulose nanocrystal–alginate hydrogel beads as novel adsorbents for organic dyes in aqueous solutions. *Cellulose*, **22**, 3725-3738.
  112. Mokhtari, A., Sabzi, M., Azimi, H., 2021. 3D porous bioadsorbents based on chitosan/alginate/cellulose nanofibers as efficient and recyclable adsorbents of anionic dye. *Carbohydrate Polymers*, **265**, 118075.
  113. Tang, J., Song, Y., Zhao, F., Spinney, S., da Silva Bernardes, J., Tam, K. C., 2019. Compressible cellulose nanofibril (CNF) based aerogels produced via a bio-inspired strategy for heavy metal ion and dye removal. *Carbohydrate Polymers*, **208**, 404-412.
  114. Sajab, M. S., Chia, C. H., Chan, C. H., Zakaria, S., Kaco, H., Chook, S. W., Chin, S. X., 2016. Bifunctional graphene oxide–cellulose nanofibril aerogel loaded with Fe (III) for the removal of cationic dye via simultaneous adsorption and Fenton oxidation. *RSC advances*, **6**, 19819-19825.
  115. Gu, J., Hu, C., Zhang, W., Dichiaro, A. B., 2018. Reagentless preparation of shape memory cellulose nanofibril aerogels decorated with Pd nanoparticles and their application in dye discoloration. *Applied Catalysis B: Environmental*, **237**, 482-490.
  116. Sai, H., Fu, R., Xing, L., Xiang, J., Li, Z., Li, F., Zhang, T., 2015. Surface modification of bacterial cellulose aerogels' web-like skeleton for oil/water separation. *ACS applied materials & interfaces*, **7**, 7373-7381.
  117. Zhang, J., Cheng, Y., Xu, C., Gao, M., Zhu, M., Jiang, L., 2021. Hierarchical Interface Engineering for Advanced Nanocellulosic Hybrid Aerogels with High Compressibility and Multifunctionality. *Advanced Functional Materials*, **31**, 2009349.
  118. Sun, L., Zhang, X., Liu, H., Liu, K., Du, H., Kumar, A., Sharma, G., Si, C., 2021. Recent Advances in Hydrophobic Modification of Nanocellulose. *Current Organic Chemistry*, **25**, 417-436.
  119. Saito, T., Isogai, A., 2004. TEMPO-mediated oxidation of native cellulose. The effect of oxidation conditions on chemical and crystal structures of the water-insoluble fractions. *Biomacromolecules*, **5**, 1983-1989.
  120. Yan, B., Ma, C., Gao, J., Yuan, Y., Wang, N., 2020. An ion-Crosslinked Supramolecular hydrogel for ultrahigh and fast uranium recovery from seawater. *Advanced Materials*, **32**, 1906615.
  121. Sluiter, A., Hames, B., Ruiz, R., Scarlata, C., Sluiter, J., Templeton, D., Crocker, D., 2010. Determination of structural carbohydrates and lignin in biomass. *Laboratory analytical procedure*.
  122. Ma, C., Gao, J., Wang, D., Yuan, Y., Wen, J., Yan, B., Zhao, S., Zhao, X., Sun, Y., Wang, X., 2019. Sunlight polymerization of poly (amidoxime) hydrogel membrane for enhanced uranium extraction from seawater. *Advanced Science*, **6**, 1900085.
  123. Rostami-Vartooni, A., Nasrollahzadeh, M., Alizadeh, M., 2016. Green synthesis of seashell supported silver nanoparticles using Bunium persicum seeds extract: application of the particles for catalytic reduction of organic dyes. *Journal of Colloid and Interface Science*, **470**, 268-275.
  124. Yang, Y., Chen, Z., Wu, X., Zhang, X., Yuan, G., 2018. Nanoporous cellulose membrane doped with silver for continuous catalytic decolorization of organic dyes. *Cellulose*, **25**, 2547-2558.

125. Vaiano, V., Sacco, O., Sannino, D., Ciambelli, P., 2015. Nanostructured N-doped TiO<sub>2</sub> coated on glass spheres for the photocatalytic removal of organic dyes under UV or visible light irradiation. *Applied Catalysis B: Environmental*, **170**, 153-161.
126. Zhang, W., Jing, Z., Shan, Y., Ge, X., Mu, X., Jiang, Y., Li, H., Wu, P., 2016. Paper reinforced with regenerated cellulose: a sustainable and fascinating material with good mechanical performance, barrier properties and shape retention in water. *Journal of Materials Chemistry A*, **4**, 17483-17490.
127. Salama, A., Shukry, N., El-Sakhawy, M., 2015. Carboxymethyl cellulose-g-poly (2-(dimethylamino) ethyl methacrylate) hydrogel as adsorbent for dye removal. *International Journal of Biological Macromolecules*, **73**, 72-75.
128. Breton, J., Boullais, C., Berger, G., Mioskowski, C., Navedryk, E., 1995. Binding sites of quinones in photosynthetic bacterial reaction centers investigated by light-induced FTIR difference spectroscopy: symmetry of the carbonyl interactions and close equivalence of the QB vibrations in *Rhodospseudomonas sphaeroides* and *Rhodobacter viridis* probed by isotope labeling. *Biochemistry*, **34**, 11606-11616.
129. Zhang, N., Zang, G.-L., Shi, C., Yu, H.-Q., Sheng, G.-P., 2016. A novel adsorbent TEMPO-mediated oxidized cellulose nanofibrils modified with PEI: preparation, characterization, and application for Cu (II) removal. *Journal of Hazardous materials*, **316**, 11-18.
130. Cai, J., Zhang, L., Chang, C., Cheng, G., Chen, X., Chu, B., 2007. Hydrogen-bond-induced inclusion complex in aqueous cellulose/LiOH/urea solution at low temperature. *ChemPhysChem*, **8**, 1572-1579.
131. Mahfoudhi, N., Boufi, S., 2017. Nanocellulose as a novel nanostructured adsorbent for environmental remediation: a review. *Cellulose*, **24**, 1171-1197.
132. Tanhaei, B., Ayati, A., Lahtinen, M., Sillanpää, M., 2015. Preparation and characterization of a novel chitosan/Al<sub>2</sub>O<sub>3</sub>/magnetite nanoparticles composite adsorbent for kinetic, thermodynamic and isotherm studies of Methyl Orange adsorption. *Chemical Engineering Journal*, **259**, 1-10.
133. Jiang, Y., Liu, B., Xu, J., Pan, K., Hou, H., Hu, J., Yang, J., 2018. Cross-linked chitosan/ $\beta$ -cyclodextrin composite for selective removal of methyl orange: Adsorption performance and mechanism. *Carbohydrate Polymers*, **182**, 106-114.
134. Jiang, X., Xiang, X., Peng, S., Hou, L., 2019. Facile preparation of nitrogen-doped activated mesoporous carbon aerogel from chitosan for methyl orange adsorption from aqueous solution. *Cellulose*, **26**, 4515-4527.
135. Obeid, L., Bée, A., Talbot, D., Jaafar, S. B., Dupuis, V., Abramson, S., Cabuil, V., Welschbillig, M., 2013. Chitosan/maghemite composite: a magsorbent for the adsorption of methyl orange. *Journal of Colloid and Interface Science*, **410**, 52-58.
136. Mahmoodian, H., Moradi, O., Shariatzadeha, B., Salehf, T. A., Tyagi, I., Maity, A., Asif, M., Gupta, V. K., 2015. Enhanced removal of methyl orange from aqueous solutions by poly HEMA-chitosan-MWCNT nano-composite. *Journal of Molecular Liquids*, **202**, 189-198.
137. Keener, M., Hunt, C., Carroll, T. G., Kampel, V., Dobrovetsky, R., Hayton, T. W., Ménard, G., 2020. Redox-switchable carboranes for uranium capture and release. *Nature*, **577**, 652-655.
138. Abney, C. W., Mayes, R. T., Saito, T., Dai, S., 2017. Materials for the recovery of uranium from seawater. *Chemical Reviews*, **117**, 13935-14013.
139. Zhao, S., Yuan, Y., Yu, Q., Niu, B., Liao, J., Guo, Z., Wang, N., 2019. A dual-surface amidoximated halloysite nanotube for high-efficiency economical uranium extraction from seawater. *Angew. Chem. Int. Edit.*, **131**, 15121-15127.

140. Ahmad, M., Wang, J., Yang, Z., Zhang, Q., Zhang, B., 2020. Ultrasonic-assisted preparation of amidoxime functionalized silica framework via oil-water emulsion method for selective uranium adsorption. *Chemical Engineering Journal*, **389**, 124441.
141. Xu, X., Zhang, H., Ao, J., Xu, L., Liu, X., Guo, X., Li, J., Zhang, L., Li, Q., Zhao, X., 2019. 3 D hierarchical porous amidoxime fibers speed up uranium extraction from seawater. *Energy Environ. Sci.*, **12**, 1979-1988.
142. Başarır, S. Ş., Bayramgil, N. P., 2013. The uranium recovery from aqueous solutions using amidoxime modified cellulose derivatives. I I I. Modification of hydroxypropylmethylcellulose with amidoxime groups. *Cellulose*, **20**, 1511-1522.
143. Li, S., Yang, P., Liu, X., Zhang, J., Xie, W., Wang, C., Liu, C., Guo, Z., 2019. Graphene oxide based dopamine mussel-like cross-linked polyethylene imine nanocomposite coating with enhanced hexavalent uranium adsorption. *J. Mater. Chem. A*, **7**, 16902-16911.
144. Wang, C., Helal, A. S., Wang, Z., Zhou, J., Yao, X., Shi, Z., Ren, Y., Lee, J., Chang, J. K., Fugetsu, B., 2021. Uranium In Situ Electrolytic Deposition with a Reusable Functional Graphene-Foam Electrode. *Advanced Materials*, **33**, 2102633.
145. Sun, Q., Aguila, B., Earl, L. D., Abney, C. W., Wojtas, L., Thallapally, P. K., Ma, S., 2018. Covalent organic frameworks as a decorating platform for utilization and affinity enhancement of chelating sites for radionuclide sequestration. *Advanced Materials*, **30**, 1705479.
146. Yu, Q., Yuan, Y., Wen, J., Zhao, X., Zhao, S., Wang, D., Li, C., Wang, X., Wang, N., 2019. A universally applicable strategy for construction of anti-biofouling adsorbents for enhanced uranium recovery from seawater. *Adv. Sci.*, **6**, 1900002.
147. Li, Q., Wu, P., Zhou, J., Zhang, L., 2012. Structure and solution properties of cyanoethyl celluloses synthesized in LiOH/urea aqueous solution. *Cellulose*, **19**, 161-169.
148. Zhou, J., Li, Q., Song, Y., Zhang, L., Lin, X., 2010. A facile method for the homogeneous synthesis of cyanoethyl cellulose in Na O H/urea aqueous solutions. *Polym. Chem.*, **1**, 1662-1668.
149. Zhao, S., Yuan, Y., Yu, Q., Niu, B., Liao, J., Guo, Z., Wang, N., 2019. A dual-surface amidoximated halloysite nanotube for high-efficiency economical uranium extraction from seawater. *Angewandte Chemie*, **131**, 15121-15127.
150. Xiong, X. H., Yu, Z. W., Gong, L. L., Tao, Y., Gao, Z., Wang, L., Yin, W. H., Yang, L. X., Luo, F., 2019. Ammoniating covalent organic framework (C O F) for high-performance and selective extraction of toxic and radioactive uranium ions. *Adv. Sci.*, **6**, 1900547.
151. Yu, Q., Yuan, Y., Wen, J., Zhao, X., Zhao, S., Wang, D., Li, C., Wang, X., Wang, N., 2019. A universally applicable strategy for construction of anti-biofouling adsorbents for enhanced uranium recovery from seawater. *Advanced Science*, **6**, 1900002.
152. Zhang, J., Zhang, H., Liu, Q., Song, D., Li, R., Liu, P., Wang, J., 2019. Diaminomaleonitrile functionalized double-shelled hollow M I L-101 (Cr) for selective removal of uranium from simulated seawater. *Chemical Engineering Journal*, **368**, 951-958.
153. Zhao, Y., Li, J., Zhao, L., Zhang, S., Huang, Y., Wu, X., Wang, X., 2014. Synthesis of amidoxime-functionalized Fe<sub>3</sub>O<sub>4</sub>@ Si O<sub>2</sub> core-shell magnetic microspheres for highly efficient sorption of U (V I). *Chemical Engineering Journal*, **235**, 275-283.
154. Cui, W. R., Li, F. F., Xu, R. H., Zhang, C. R., Chen, X. R., Yan, R. H., Liang, R. P., Qiu, J. D., 2020. Regenerable Covalent Organic Frameworks for Photo-enhanced Uranium Adsorption from Seawater. *Angew. Chem. Int. Edit.*, **132**, 17837-17843.
155. Pan, H.-B., Liao, W., Wai, C. M., Oyola, Y., Janke, C. J., Tian, G., Rao, L., 2014. Carbonate-H<sub>2</sub>O<sub>2</sub> leaching for sequestering uranium from seawater. *Dalton Trans.*, **43**, 10713-10718.
156. Wu, J., Tian, K., Wang, J., 2018. Adsorption of uranium (V I) by amidoxime modified multiwalled carbon nanotubes. *Prog. Nucl. Energ.*, **106**, 79-86.

157. Wang, X. L., Li, Y., Huang, J., Zhou, Y. Z., Li, B. L., Liu, D. B., 2019. Efficiency and mechanism of adsorption of low concentration uranium in water by extracellular polymeric substances. *J. Environ. Radioactiv.*, **197**, 81-89.
158. Sperry, J. S., 2003. Evolution of water transport and xylem structure. *International Journal of Plant Sciences*, **164**, S115-S127.
159. Kitin, P., Funada, R., 2016. Earlywood vessels in ring-porous trees become functional for water transport after bud burst and before the maturation of the current-year leaves. *Iawa Journal*, **37**, 315-331.
160. Li, Q., Wu, P., Zhou, J., Zhang, L., 2012. Structure and solution properties of cyanoethyl celluloses synthesized in Li O H/urea aqueous solution. *Cellulose*, **19**, 161-169.
161. Qi, H., Cai, J., Zhang, L., Kuga, S., 2009. Properties of films composed of cellulose nanowhiskers and a cellulose matrix regenerated from alkali/urea solution. *Biomacromolecules*, **10**, 1597-1602.
162. Jia, C., Shao, Z., Fan, H., Feng, R., Wang, F., Wang, W., Wang, J., Zhang, D., Lv, Y., 2016. Barium titanate as a filler for improving the dielectric property of cyanoethyl cellulose/antimony tin oxide nanocomposite films. *Composites Part A: Applied Science and Manufacturing*, **86**, 1-8.
163. Sehaqui, H., Salajková, M., Zhou, Q., Berglund, L. A., 2010. Mechanical performance tailoring of tough ultra-high porosity foams prepared from cellulose I nanofiber suspensions. *Soft Matter*, **6**, 1824-1832.
164. Seantier, B., Bendahou, D., Bendahou, A., Grohens, Y., Kaddami, H., 2016. Multi-scale cellulose based new bio-aerogel composites with thermal super-insulating and tunable mechanical properties. *Carbohydrate Polymers*, **138**, 335-348.
165. Zhang, X., Wang, H., Cai, Z., Yan, N., Liu, M., Yu, Y., 2018. Highly compressible and hydrophobic anisotropic aerogels for selective oil/organic solvent absorption. *ACS Sustainable Chemistry & Engineering*, **7**, 332-340.
166. Zhang, X., Wang, Y., Zhao, J., Xiao, M., Zhang, W., Lu, C., 2016. Mechanically strong and thermally responsive cellulose nanofibers/poly (N-isopropylacrylamide) composite aerogels. *ACS Sustainable Chemistry & Engineering*, **4**, 4321-4327.
167. Xiao, S., Gao, R., Lu, Y., Li, J., Sun, Q., 2015. Fabrication and characterization of nanofibrillated cellulose and its aerogels from natural pine needles. *Carbohydrate Polymers*, **119**, 202-209.
168. Sehaqui, H., Zhou, Q., Berglund, L. A., 2011. High-porosity aerogels of high specific surface area prepared from nanofibrillated cellulose (NFC). *Composites Science and Technology*, **71**, 1593-1599.
169. Liu, A., Medina, L., Berglund, L. A., 2017. High-strength nanocomposite aerogels of ternary composition: poly (vinyl alcohol), clay, and cellulose nanofibrils. *ACS applied materials & interfaces*, **9**, 6453-6461.
170. Pircher, N., Carbajal, L., Schimper, C., Bacher, M., Rennhofer, H., Nedelec, J.-M., Lichtenegger, H. C., Rosenau, T., Liebner, F., 2016. Impact of selected solvent systems on the pore and solid structure of cellulose aerogels. *Cellulose*, **23**, 1949-1966.
171. Pääkkö, M., Vapaavuori, J., Silvennoinen, R., Kosonen, H., Ankerfors, M., Lindström, T., Berglund, L. A., Ikkala, O., 2008. Long and entangled native cellulose I nanofibers allow flexible aerogels and hierarchically porous templates for functionalities. *Soft Matter*, **4**, 2492-2499.
172. Sai, H., Xing, L., Xiang, J., Cui, L., Jiao, J., Zhao, C., Li, Z., Li, F., Zhang, T., 2014. Flexible aerogels with interpenetrating network structure of bacterial cellulose–silica composite from sodium silicate precursor via freeze drying process. *Rsc Advances*, **4**, 30453-30461.
173. Schestakow, M., Karadagli, I., Ratke, L., 2016. Cellulose aerogels prepared from an aqueous zinc chloride salt hydrate melt. *Carbohydrate Polymers*, **137**, 642-649.

174. Chen, B., Zheng, Q., Zhu, J., Li, J., Cai, Z., Chen, L., Gong, S., 2016. Mechanically strong fully biobased anisotropic cellulose aerogels. *RSC advances*, **6**, 96518-96526.
175. Liu, S.-C., Wu, M.-B., Ye, H., Liu, L., Ma, L.-L., Yao, J., 2021. Amidoximated cellulose microspheres synthesized via homogenous reactions for High-Performance extraction of uranium from seawater. *Chemical Engineering Journal*, **426**, 131378.
176. S., Das, W.-P., Liao, M., Flicker, Byers, C., Tsouris, C., 2016. Alternative Alkaline Conditioning of Amidoxime Based Adsorbent for Uranium Extraction from Seawater. *Industrial & Engineering Chemistry Research*.
177. Joanna, Gorka, Richard, T., Mayes, Loic, Baggetto, 2013. Sonochemical functionalization of mesoporous carbon for uranium extraction from seawater. *Journal of Materials Chemistry A Materials for Energy & Sustainability*.
178. Wu, J., Tian, K., Wang, J., 2018. Adsorption of uranium (VI) by amidoxime modified multiwalled carbon nanotubes. *Progress in Nuclear Energy*, **106**, 79-86.
179. Pan, H.-B., Liao, W., Wai, C. M., Oyola, Y., Janke, C. J., Tian, G., Rao, L., 2014. Carbonate-H<sub>2</sub>O<sub>2</sub> leaching for sequestering uranium from seawater. *Dalton transactions*, **43**, 10713-10718.

